

On the Dust properties of the UV galaxies in the redshift range $z \sim 0.6 - 1.2$

M. Sharma^{1,2*}, M. J. Page¹, M. Symeonidis¹, I. Ferreras^{3,4,5}

¹Mullard Space Science Laboratory, University College London, Holmbury St Mary, Dorking, Surrey, RH5 6NT, UK

²Isaac Newton Group of Telescopes, C. Álvarez Abreu, 70, E38700 Santa Cruz de La Palma, La Palma, Spain

³Instituto de Astrofísica de Canarias, Calle Vía Láctea s/n, E38205, La Laguna, Tenerife, Spain

⁴Departamento de Astrofísica, Universidad de La Laguna, E38206, La Laguna, Tenerife, Spain

⁵Department of Physics and Astronomy, University College London, Gower Street, London WC1E 6BT, UK

Accepted 2024 January 09; Received 2024 January 08; in original form 2023 November 14

ABSTRACT

Far-infrared observations from the *Herschel Space Observatory* are used to estimate the infrared (IR) properties of ultraviolet-selected galaxies. We stack the PACS (100, 160 μm) and SPIRE (250, 350 and 500 μm) maps of the Chandra deep field south (CDFS) on a source list of galaxies selected in the rest-frame ultraviolet (UV) in a redshift range of 0.6–1.2. This source list is created using observations from the XMM-OM telescope survey in the CDFS using the UVW1 (2910 Å) filter. The stacked data are binned according to the UV luminosity function of these sources, and the average photometry of the UV-selected galaxies is estimated. By fitting modified black bodies and IR model templates to the stacked photometry, average dust temperatures and total IR luminosity are determined. The luminosity-weighted average temperatures are consistent with a weak trend of increasing temperature with redshift found by previous studies. Infrared excess, unobscured, and obscured star formation rate (SFR) values are obtained from the UV and IR luminosities. We see a trend in which dust attenuation increases as UV luminosity decreases. It remains constant as a function of IR luminosities at fixed redshift across the luminosity range of our sources. In comparison to local luminous infrared galaxies with similar SFRs, the higher redshift star-forming galaxies in the sample show a lesser degree of dust attenuation. Finally, the inferred dust attenuation is used to correct the unobscured SFR density in the redshift range 0.6–1.2. The dust-corrected SFR density is consistent with measurements from IR-selected samples at similar redshifts.

Key words: galaxies: star formation — galaxies: luminosity function — infrared: galaxies — ultraviolet: galaxies

1 INTRODUCTION

Star formation is controlled by various fundamental processes and is one of the key global mechanisms for galaxy evolution. It has shaped the galaxies as we observe them today. In other words, it plays a crucial role in the evolutionary history of galaxies, and constraining the star formation rate (SFR) is important for understanding this evolution.

The ultraviolet (UV) continuum in the spectral energy distribution (SED) of star-forming galaxies is produced by young massive stars, and it is widely used as one of the most important indicators of the SFR (Kennicutt & Evans 2012). It has been employed by studies constraining the luminosity density in the nearby Universe (e.g. Wyder et al.

2005; Budavári et al. 2005) as well as at low (e.g. Sullivan et al. 2000), intermediate (e.g. Oesch et al. 2010; Page et al. 2021; Sharma et al. 2022) and high redshifts (Parsa et al. 2016; Bouwens et al. 2015; Donnan et al. 2023). The UV continuum can also be produced by AGN, which makes it important to consider their identification in a sample of star-forming galaxies under consideration.

Rest frame UV radiation is particularly susceptible to being obscured by dust in star-forming regions of a galaxy. The UV flux is scattered and/or absorbed by dust particles, which then reemit this energy as thermal black-body radiation in the far-infrared (FIR) wavelength range. In the local Universe, for near-UV (NUV) selected sources Buat et al. (2005) and Burgarella et al. (2006) found the typical dust attenuation in far-UV (FUV) to be 1.1 and 1.4 mags, respectively. The effect becomes more severe with an increase in

* E-mail: mnushv@gmail.com (MS)

redshift and a larger fraction of UV radiation is absorbed by dust at higher redshifts compared to the local Universe. According to a study by [Takeuchi et al. \(2005\)](#), the portion of the far-UV SFR that is obscured by dust increases from 56 per cent in the nearby Universe to 84 per cent at an average redshift of 1. Therefore, correcting UV luminosities for dust attenuation is essential before it can be used to estimate the SFR.

One of the suggested methods to solve this issue of dust attenuation involves utilizing the empirical correlation between UV dust attenuation (A_{FUV}) and the slope (β) of the UV continuum described by a power law ($f_{\lambda} \propto \lambda^{\beta}$; [Calzetti et al. 1994, 2000](#); [Meurer et al. 1999](#); [Overzier et al. 2010](#)). To quantify the UV attenuation, this approach involves the ratio of the FIR to the UV luminosity, also known as the infrared (IR) excess or IRX. Many studies that rely solely on UV data have utilised this relationship as a standard practise in order to correct their estimates of SFR or luminosity density (LD) for the effects of dust attenuation (e.g. [Schiminovich et al. 2005](#); [Bouwens et al. 2009](#); [Finkelstein et al. 2012](#); [Bouwens et al. 2015, 2020](#)).

The central concept underlying this approach is that all galaxies possess the same intrinsic spectral slope (β), which can only be altered by the presence of dust obscuration. While this assumption may seem to hold in the nearby Universe ([Meurer et al. 1999](#)), the spectral slope can also be influenced by a variety of other factors, including the redshift, the initial mass function (IMF), the metallicity, and other quantities, in addition to dust obscuration ([Wilkins et al. 2012a,b](#); [Tress et al. 2018](#)). In addition, the UV continuum slope is generally bluer than the assumed inherent value in the Meurer relation ([Wilkins et al. 2013](#)). As a result of these various factors, this relation, which was initially calibrated for starburst galaxies ([Meurer et al. 1999](#)), may be subject to modification when applied to normal galaxies, depending on various global factors such as age (e.g. [Reddy et al. 2012](#); [Narayanan et al. 2018](#)), stellar mass ([Reddy et al. 2010, 2018](#); [Fudamoto et al. 2020](#)), luminosity, and SFR of the galaxy (e.g. [Casey et al. 2014](#)). Furthermore, this relationship has been found to be influenced by local properties such as the geometry of the dust-emitting region (e.g. [Witt & Gordon 2000](#); [Narayanan et al. 2018](#)), and it has been discovered that the specific shape of this relationship can depend on the extinction law (e.g. [Narayanan et al. 2018](#)) and the source selection criteria ([Buat et al. 2005](#)).

The other more direct and reliable way to measure dust attenuation is through IRX, which is calculated as the ratio of the luminosity in the IR region to the luminosity in the ultraviolet region of the SEDs of the galaxy ([Meurer et al. 1999](#)). This method works because dust absorbs UV light and re-emits it as thermal radiation in the IR bands. By measuring the IR emission, it is possible to determine how much UV light has been absorbed by dust. This information can be used to correct UV/optical observations for dust attenuation, and the FIR flux can also be used as a proxy for the amount of obscured star formation in a galaxy. ([Buat 1992](#); [Xu & Buat 1995](#); [Meurer et al. 1995](#); [Heckman et al. 1998](#); [Gordon et al. 2000](#)). Additionally, the use of both UV and IR observations provides a way to trace both attenuated and unattenuated star formation in a galaxy as a composite measure of star formation ([Calzetti et al. 2007](#)).

The IRX ratio is based on the relative brightness of ul-

traviolet (UV) radiation that has not been absorbed by dust in a system compared to the FIR radiation that has been absorbed and reemitted by dust. The basic premise behind the IRX ratio is that there should be a balance between the UV/optical light absorbed by dust and the FIR radiation emitted ([Buat & Xu 1996](#); [Buat et al. 1999](#)). However, this balance may not always be straightforward in practise and may be influenced by the age of the dust heating system. Although this method has the advantage of being independent of other IR properties and star-dust geometry ([Gordon et al. 2000](#); [Witt & Gordon 2000](#); [Cortese et al. 2008](#)), it is not as widely used as the previous method based on the Meurer relation due to the ease of accessing data to calculate the UV spectral slope and the lack of deep FIR data at high redshifts. However, if deep FIR data is available, the IRX method can be a powerful tool for studying dust attenuation in different types of systems ([Buat et al. 1999](#)) and may provide more robust results than the other method that relies on more uncertain assumptions.

The method of using the IRX ratio to estimate dust attenuation in galaxies has been widely studied in the literature. A study using this method, conducted by [Buat et al. \(2005\)](#), analysed a sample of galaxies selected by the *Galaxy Evolution Explorer (GALEX)* in the near-ultraviolet (NUV) band and *Infrared Astronomy Satellite (IRAS)* data at 60 μm , and found that the mean dust attenuation in the FUV was 1.6 magnitudes in the nearby Universe. Other studies have extended this to higher redshifts, finding that the IRX ratio as a function of bolometric luminosity ($L_{\text{IR}} + L_{\text{UV}}$) of the galaxies evolves to redshift 1 for Lyman break galaxies ([Burgarella et al. 2007](#)) and redshift 2 for BM/BX galaxies ([Reddy et al. 2006](#)). However, [Buat et al. \(2009\)](#) did not see a clear evolution in the IRX ratio at fixed bolometric luminosity up to a redshift of 1 in their homogeneously selected sample of galaxies from *GALEX*, and suggested that it might be more useful to look at the IRX ratio as a function of UV luminosity rather than bolometric luminosity.

One challenge in studying the dust attenuation in galaxies at high redshifts is the availability of FIR data, as current IR telescopes have limited sensitivity and resolution, making these observations scarce and restricted to the most massive galaxies. Stacking analysis, in which multiple data with a lower signal-to-noise ratio are combined to increase the overall signal-to-noise ratio ([Dole et al. 2006](#); [Marsden et al. 2009](#); [B  thermin et al. 2010](#); [Kurczynski & Gawiser 2010](#); [Roseboom et al. 2012](#); [Viero et al. 2013](#)), has been used in some studies to estimate the UV attenuation due to dust at higher redshifts.

Some examples of studies that have used stacking analysis to estimate UV attenuation due to dust at higher redshifts include those by [Xu et al. \(2007\)](#), who extended IRX-based dust attenuation estimates to redshift 0.6 using data from the *GALEX* survey and the *Spitzer Space Telescope* at 24 μm , and [Heinis et al. \(2013\)](#), who used data from the Canada-France-Hawaii Telescope (CFHT) u^* -band imaging in the Cosmic Evolution Survey (COSMOS) field to estimate IRX at redshift ~ 1.5 . They found mean IRX to be 6.6 and 6.9 respectively. These measurements were taken to redshifts around 2 by [Reddy et al. \(2012\)](#), who used UV-selected galaxies from the Low-Resolution Imaging Spectrograph (LRIS) on the Keck telescope ([Steidel et al. 2004](#); [Reddy et al. 2006](#)) and obtained an IRX value of 7.1, indi-

cating that only 20 per cent of the star formation is not dust obscured.

Other works have also studied the IRX ratio at higher redshifts with stacking methods on different data sets. [Álvarez-Márquez et al. \(2016\)](#) calculated the IRX ratio at redshift ~ 3 using u^* , V_J and i^+ band imaging and *Herschel Space Observatory* (hereafter *Herschel*) maps in the COSMOS field and estimated an average value of 7.9. Using Lyman break galaxy candidates at average redshifts 3.8 from the NOAO Deep Wide-Field Survey of the Boötes field, [Lee et al. \(2012\)](#) found IRX values of 3 to 4, implying that 30 to 40 per cent of the star formation occurs without any dust attenuation. More recently, [Reddy et al. \(2018\)](#) used the *Hubble Space Telescope (HST)* data from the 3D-HST survey ([Skelton et al. 2014](#)) and the Hubble Deep UV (HDUV) Legacy Survey ([Oesch et al. 2018](#)), along with *Spitzer* MIPS 24 μm and *Herschel* PACS 100 and 160 μm data, to calculate an average IRX value of 2.94 for redshifts between 1.5 and 2.5 in the Great Observatories Origins Deep Survey (GOODS) fields.

For redshifts up to 1, similar studies have been performed using only *GALEX* data for UV selection, which can be subjected to issues related to source confusion due to its poor spatial resolution. More studies are needed to revisit this redshift range with better data and determine whether the trend observed in previous studies holds at these intermediate redshifts.

In this study, we used the UV-selected sample ([Sharma et al. 2022](#)) of galaxies from the Chandra Deep Field South (CDFs) survey of the *XMM-Newton* Optical Monitor (XMM-OM, Optical Monitor; [Mason et al. 2001](#)) onboard the *XMM-Newton* observatory. The UVW1 filter ($\lambda_{\text{eff}} = 2910 \text{ \AA}$) of the XMM-OM telescope provides rest-frame 1500 \AA imaging in the redshift range of our interest (0.6–1.2), over a field of view of 17×17 sq. arcminutes. These galaxies are stacked on the FIR maps at 100, 160, 250, 350 and 500 μm from *Herschel* to obtain the average FIR flux of the galaxies in bins of the UV luminosity function created for these galaxies by [Sharma et al. \(2022\)](#). Using the integrated IR luminosity we calculate the IRX ratio and then use it to calculate the dust attenuation of the FUV radiation, which in turn is used to correct the SFR density (SFRD) calculated using the UV measurements of [Sharma et al. \(2022\)](#).

This paper is structured as follows. The data used in this work are explained in Section 2. We describe our methods in Section 3. In particular the deblending process for the SPIRE maps in Section 3.1, stacking the FIR maps and extraction of the average photometry from the stacks in Section 3.2, fitting the IR model templates to the average IR flux densities and the estimation of dust properties like total IR luminosity and dust temperature in Section 3.3. We discuss the methods to obtain the star formation rates (unobscured and obscured using the UV and FIR tracers) and the average dust attenuation of the UV light in Sections 3.4 and 3.5. We summarise our results in Section 4 and discuss their implications in Section 5. Finally, we conclude this paper in Section 6. Throughout the paper, we adopt a flat cosmology with $\Omega_\Lambda = 0.7$, $\Omega_M = 0.3$ and Hubble’s constant $H_0 = 70 \text{ km s}^{-1} \text{ Mpc}^{-1}$. The distances (and volumes) are calculated in comoving coordinates in Mpc (and Mpc^3). We use the AB system of magnitudes ([Oke & Gunn 1983](#)). The

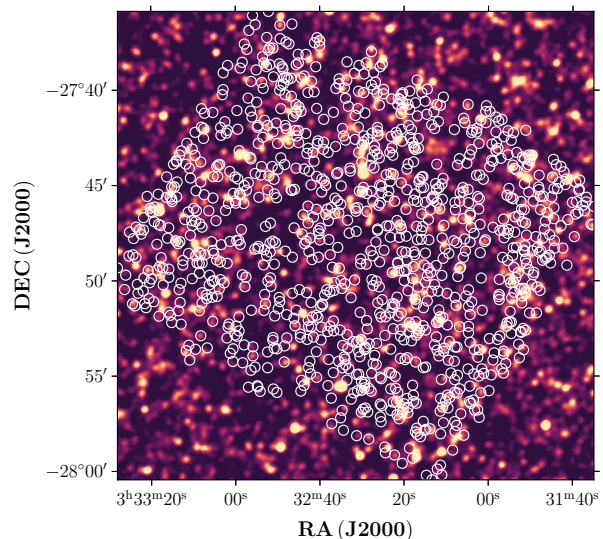


Figure 1. The UV source positions overlaid on the 250 μm SPIRE map. A total of 1070 sources (ignoring UV bins with < 25 sources) with a S/N above 3, from an area ~ 400 sq. arcmins in the CDFS are used in this study.

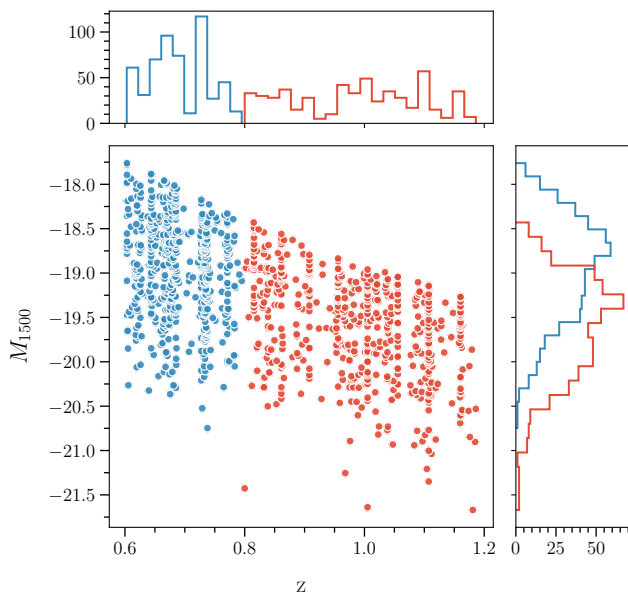


Figure 2. Rest frame UV (M_{1500}) absolute magnitudes and redshift distribution of the UVW1 sources stacked in this study. Blue and red colours represent the sources in the redshift bin centered at 0.7 and 1.0 respectively. The faint magnitude end of the distribution is truncated because of the apparent magnitude limit of our flux-limited survey in the CDFS. The apparent magnitude limit is UVW1 = 24.5 mag.

FIR luminosities are integrated over $8 - 1000 \mu\text{m}$, and the FUV luminosities are defined as λL_λ , where $\lambda = 1500 \text{ \AA}$.

2 DATA

For this study, we have employed the data products obtained from the XMM-OM and *Herschel* telescopes, specif-

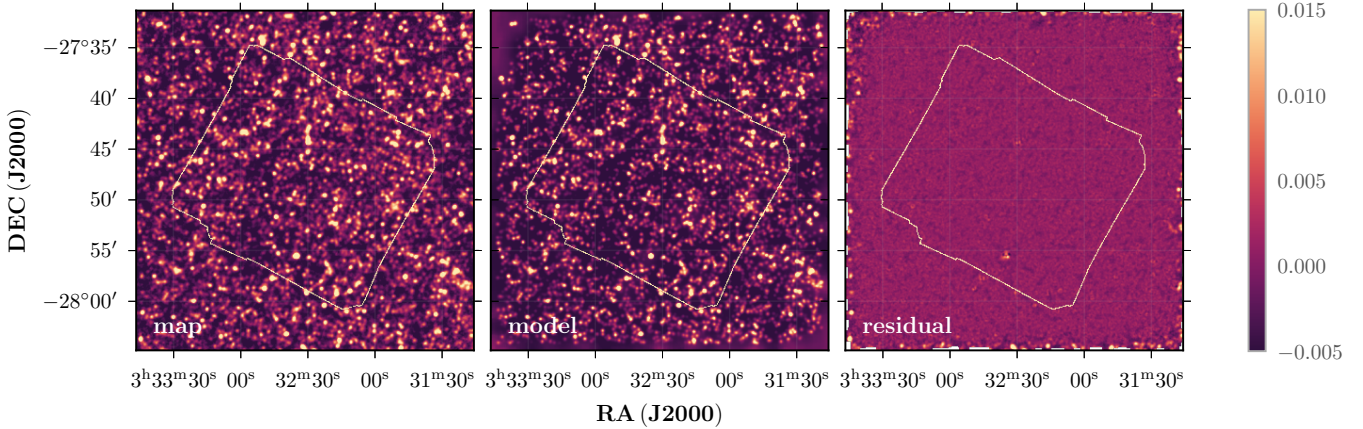


Figure 3. We depict the deblending process here as described in Section 3 with an example of the $250\ \mu\text{m}$ map from *Herschel* SPIRE. The *left* panel shows the original map. In the *middle* panel we show our model for the $250\ \mu\text{m}$ map, and the *right* hand panel shows the residual map created by subtracting the model from the original map. The colour bar represents the pixel values of the flux density calibrated in units of Jy/beam .

Table 1. Properties of the *Herschel* SPIRE and PACS data used in this study. The 1σ noise for the SPIRE maps is the total noise including both the instrumental and confusion components.

Central λ (μm)	Pixel Scale (arcsec)	FWHM (arcsec)	3σ depth (mJy)
100	1.2	7.2	4.50 ^a
160	2.4	12	8.50 ^a
250	6.0	18.15	6.72 ^b
350	8.33	25.15	5.58 ^b
500	12.0	36.30	8.04 ^b

^aFrom Gruppioni et al. (2013).

^bFrom Viero et al. (2013).

ically focusing on the Chandra Deep Field South (CDFs). This particular field, which is centred at RA 3h 32m 28.0s DEC $-27^\circ 48' 30''$ (J2000.0) (Rosati et al. 2002) in the southern sky, has been the primary target of observation for the Chandra X-ray Observatory (Luo et al. 2008). Over the last two decades, this field has been the subject of extensive observation through a variety of multi-wavelength surveys, and as such, a plethora of ancillary information has been accumulated.

2.1 UV selected galaxies in the CDFS

The UVW1 filter, characterised by an effective wavelength of $2910\ \text{\AA}$, of the XMM-OM, can be used to generate samples that comprise star-forming galaxies in the redshift range of 0.6 to 1.2. This has been demonstrated in studies conducted in the 13 Hr field (Page et al. 2021), as well as in the CDFS (Sharma et al. 2022) and COSMOS (Sharma et al. 2023, submitted) fields. In the aforementioned study Sharma et al. (2022), we used the UV imaging capabilities of the XMM-OM. The CDFS was observed over a decade, from 2001 to 2010 using the UVW1 filter. The data from this extensive observing campaign enabled us to create a deep ultraviolet

image of the CDFS, which covers an area of approximately 400 sq. arcminutes. This image was subsequently used to create a source list of galaxies by extracting photometry in the rest frame $1500\ \text{\AA}$, spanning a redshift range of 0.6–1.2. The UVW1 filter can also select stars and AGNs due to their UV emissions. Quasars in particular, where the UV radiation from the accretion disc around the supermassive black hole outshines the stars in the host galaxy, could contaminate our samples. Such AGN as well as the stars have been removed using their X-ray emission. By leveraging supplementary data from other catalogues within the CDFS, a UV catalogue that comprised 1079 galaxies, with a signal-to-noise of > 3 , was compiled. The sources of the supplementary data are mentioned in Section 4.2 and a list of catalogues used for photometric and spectroscopic redshifts is provided in Table 2 of Sharma et al. (2022). The sample produced through this process is used in this investigation to study the average IR properties of these star-forming galaxies. Figure 2 shows this sample in the rest-frame magnitude-redshift space.

2.2 FIR observations of the CDFS

The data used in this analysis are sourced from *Herschel* (Pilbratt et al. 2010), specifically utilising data taken by the Spectral and Photometric Imaging Receiver (SPIRE; Griffin et al. 2010) and the Photodetector Array Camera and Spectrometer (PACS; Poglitsch et al. 2010) instruments.

2.2.1 *Herschel* SPIRE

The SPIRE data were obtained at $250\ \mu\text{m}$, $350\ \mu\text{m}$, and $500\ \mu\text{m}$ as part of the *Herschel* Multi-tiered Extragalactic Survey (HerMES; Oliver et al. 2012). The maps used in this analysis were taken from HeDam¹ and were observed to a

¹ <https://hedam.lam.fr/HerMES/index/dr4>

3σ depth of 6.72, 5.58, and 8.04 mJy, respectively, without taking into account confusion noise (Viero et al. 2013). The confusion noise for these SPIRE maps, as calculated by Nguyen et al. (2010), is determined to be 5.8, 6.3, and 6.8 mJy at 1σ level for the 250 μm , 350 μm , and 500 μm filters, respectively. Therefore, these maps, due to their larger beam size, are limited by confusion noise. In Figure 1, we present a plot of our UV source list, which is overlaid on top of the 250 μm map that was obtained from the SPIRE instrument.

2.2.2 Herschel PACS

The PACS data were obtained as part of the PACS Evolutionary Probe survey (PEP²; Lutz et al. 2011), at wavelengths of 100 μm and 160 μm . The particular area of the sky that is the focus of our analysis, characterised by UVW1 sources, is observed as part of the Extended Chandra Deep Field South leg of the PEP survey. The overall field has been observed to a 3σ depths of 4.5 and 8.5 mJy (Gruppioni et al. 2013). It is worth noting that a portion of the field covered by our sources, specifically the GOODS-S region, is observed to deeper fluxes (1.2 and 2.4 mJy at the 3σ level). However, for the purpose of maintaining uniformity in terms of depth for all sources, these deeper data have not been included in the present analysis. In contrast to the SPIRE maps, which are limited by confusion noise, the PACS maps, due to their small beam size, are limited by instrumental noise.

3 METHODS

3.1 Deblending SPIRE maps

When there are a large number of sources situated in close proximity to each other, it can be challenging to accurately distinguish and identify them as individual entities. This situation can arise when the sources are so close to each other that they appear to blend together and appear as a single source. This can have a significant impact on source identification and compromise the accuracy of the identified source positions, which in turn affects the cross-matching with other catalogues. When two or more sources are blended together, the measurements of flux density can be overestimated, which can skew the calculations of derived estimates such as dust temperatures and total IR luminosities. In addition, when sources appear separated but are still close together, the emission from the wings of one source may be incorrectly attributed to another nearby source. The SPIRE instrument, in particular, is affected by this blending due to its coarse beam, and, as a result, its FIR maps need to be corrected before they can be used to calculate flux densities. Furthermore, the clustering of sources in the IR sky can have a significant impact on the stacking measurements performed on such sources, as it has the potential to contribute at the wings of the stacked signals and thus boost the overall flux (Dole et al. 2006; Béthermin et al. 2010; Kurczynski & Gawiser 2010; Béthermin et al. 2012; Heinis et al. 2013; Álvarez-Márquez et al. 2016). In particular, Béthermin et al. (2012) carried out an estimation of clustering contribution for a sample selected at 24 μm , and found that stacked flux

measurements are boosted by approximately 8, 10, and 19 per cent at 250, 350 and 500 μm , respectively.

To address these issues, we employ a technique known as deblending to correct the SPIRE maps. The basic concept behind this process is relatively straightforward. We model the SPIRE maps using the positions of sources in the 24 μm and radio catalogues, under the assumption that the majority of sources detected in the SPIRE (250, 350 and 500 μm) bands should have a corresponding detection in these bands. To this end, a comprehensive prior catalogue is created utilising the 24 μm catalogue of the CDFS as part of the Far-Infrared Deep Extra-galactic Legacy (FIDEL) Survey. For the area of the CDFS that overlaps with GOODS-South, we use a more detailed and deep catalogue from Magnelli et al. (2011) in place of the sources from the CDFS. However, it is important to note that some of the SPIRE sources may not have been detected in the 24 μm band, thus, to make the prior catalogue as complete as possible, radio catalogues from Miller et al. (2013) and Franzen et al. (2015) are also employed. For the 250 and 350 μm bands, we use sources that are brighter than 30 μJy and have a signal-to-noise ratio of at least 3 and 5, respectively, from the FIDEL and GOODS-S catalogues. To avoid over-deblending of the 500 μm maps, it is necessary to use a source list with a relatively low number density of sources. To accomplish this, we create a separate prior source list specifically for the 500 μm maps by applying more stringent constraints to the 24 μm FIDEL and GOODS-S 24 μm catalogues. For the 500 μm prior list, we use sources with fluxes $> 40 \mu\text{Jy}$ at 5σ for both the FIDEL and GOODS-S catalogues.

The deblending process is performed in two steps, with the first step using the prior catalogue to produce an initial set of models for the SPIRE maps. However, it is likely that some sources may still be missed due to the incompleteness of the prior catalogues. So, in order to improve our models, we undertake a second run of the process, this time utilising a modified prior catalogue. Any sources missing from the initial catalogue are identified through source detection in the residual maps produced in the first step. This is accomplished using SExtractor (Bertin & Arnouts 1996) with a detection threshold of 3, 3.5 and 4σ , respectively, for the 250, 350 and 500 μm maps. These newly detected sources are then added to the original catalogue, and the entire modelling process is re-run. The resulting models, along with the original and residual maps from the second run, are illustrated in Figure 3 (for the 250 μm band). The equivalent Figures for 350 and 500 μm are shown in Appendix A. Similar methods have been used in several previous studies, such as those conducted by Swinbank et al. (2014), Thomson et al. (2017), and Liu et al. (2018).

The sources in the final prior catalogue that are also present in the UV source list are added back to the residual maps to preserve their FIR contribution because, as explained in the next Section, the stacking and average photometry are performed on the residual maps.

3.2 Stacking FIR maps

Astronomical imaging at long wavelengths, such as FIR and sub-millimeter, is often hindered by high levels of noise. Additionally, the point spread function (PSF) is large at these wavelengths, which means that individual sources appear to

² <https://www.mpe.mpg.de/ir/Research/PEP/DR1>

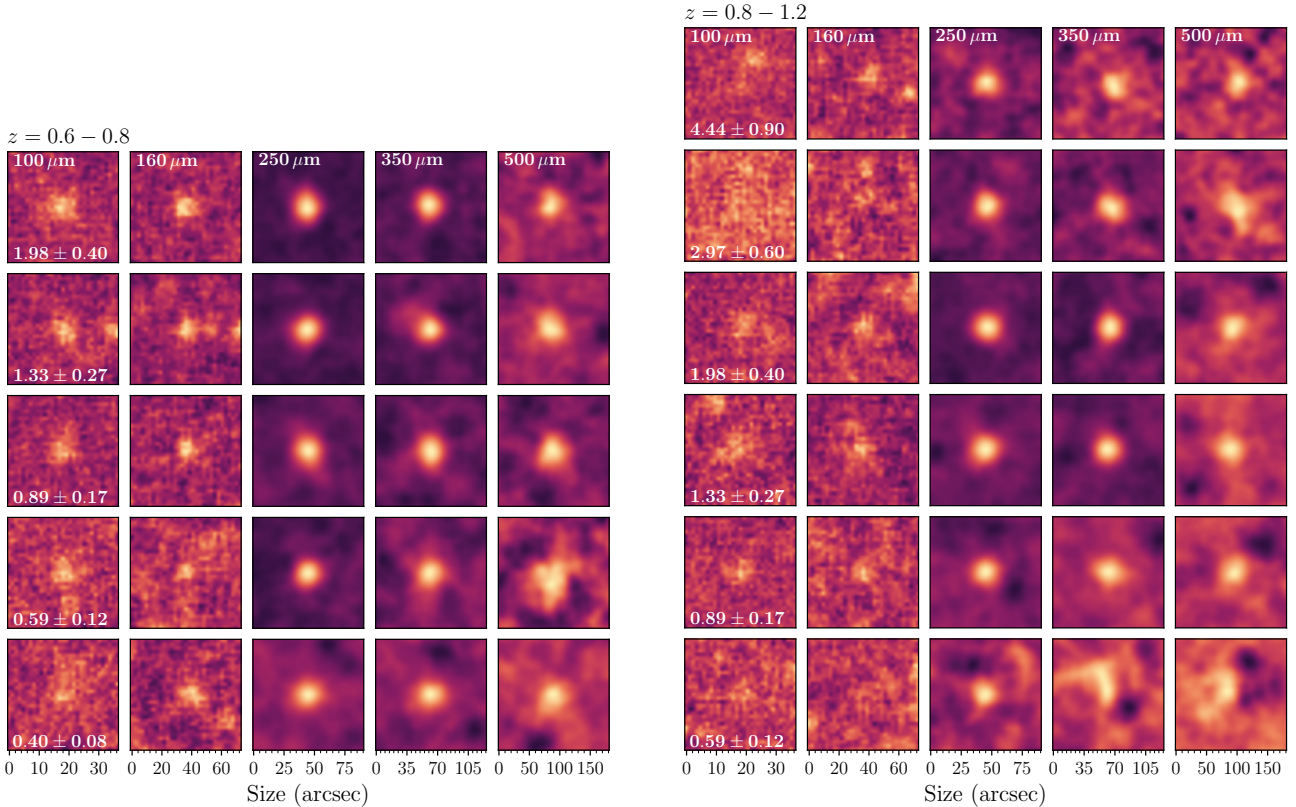


Figure 4. The PACS and SPIRE stacks used in this work for redshift range 0.6-0.8 (on the left) and 0.8-1.2 (on the right). The first two columns represent the PACS 100 and 160 μm band and the last three columns represent respectively the *Herschel* waveband (from 100 to 500 μm) they represent. Each row represents a UV luminosity bin in descending order of UV luminosity from top to bottom. These UV luminosities of the UV LF bins are labelled in the first (leftmost) stack of each row in units of $\times 10^{10} L_{\odot}$. Table 3 lists the UV luminosity, and IR luminosity of each UV luminosity bin along with the number of sources stacked to produce these stacks. The size of the stacks in arcseconds is labelled on the bottom edge of each stack in the bottom row. Every stack has a total width roughly 5 times the FWHM. Due to the different pixel scales of the maps each map has a different size in arcseconds.

spread out and blend together. This makes it difficult to resolve individual sources and determine the fluxes of each source. One way to overcome this is to use stacking analysis, a technique that utilises the improved positional accuracy of short-wavelength catalogues from the same region of the sky as the long-wavelength imaging. These catalogues can be used to identify the positions of sources that are likely to be present in the long-wavelength images. Using this positional information, one can extract fluxes at the prior source positions from the long-wavelength maps. By averaging the fluxes of many sources together, the stacking process results in an improved signal-to-noise ratio (S/N) by a factor of $1/\sqrt{N}$, where N is the number of sources averaged and assuming that the individual sources have the same S/N. This improvement in the S/N ratio makes it possible to extract information about faint sources that would otherwise be hidden in the noise, and impossible to detect.

In our case, we used the prior positions of the UV-selected galaxies from the UVW1 source list from [Sharma et al. \(2022\)](#). We stack our UVW1 sources on the (stacking) bias-corrected PACS maps. However, for SPIRE maps, we use the residual maps coming out of the deblending process, which are corrected for issues related to confusion noise and clustering. The stacking of residual maps should give results

consistent with the stacking of the actual maps, as demonstrated by [Reddy et al. \(2012\)](#), with the advantage of a lower noise level or uncertainty than the stacking of the actual maps.

3.2.1 Stacking Process

We take small square Sections (“stamps”) from the SPIRE and PACS maps at the predefined location of each UV-selected source. The dimensions of these square stamps, which are centred on the prior position of each UV-selected source, are $S \times S$, where S is approximately 5 times the full width at half-maximum (FWHM) of the corresponding *Herschel* map. Once the stamps have been extracted, we then proceed to sort them into UV luminosity bins based on the UV luminosity function from [Sharma et al. \(2022\)](#). To ensure that our statistics are robust and reliable, we remove bins that contain less than 25 sources. As a result of this process, we are left with a collection of data cubes, each cube corresponding to a specific bin in the UV LF. Subsequently, we collapse these data cubes by averaging the pixel values of all the stacked stamps contained within each bin. This process yields a stacked average image for every bin.

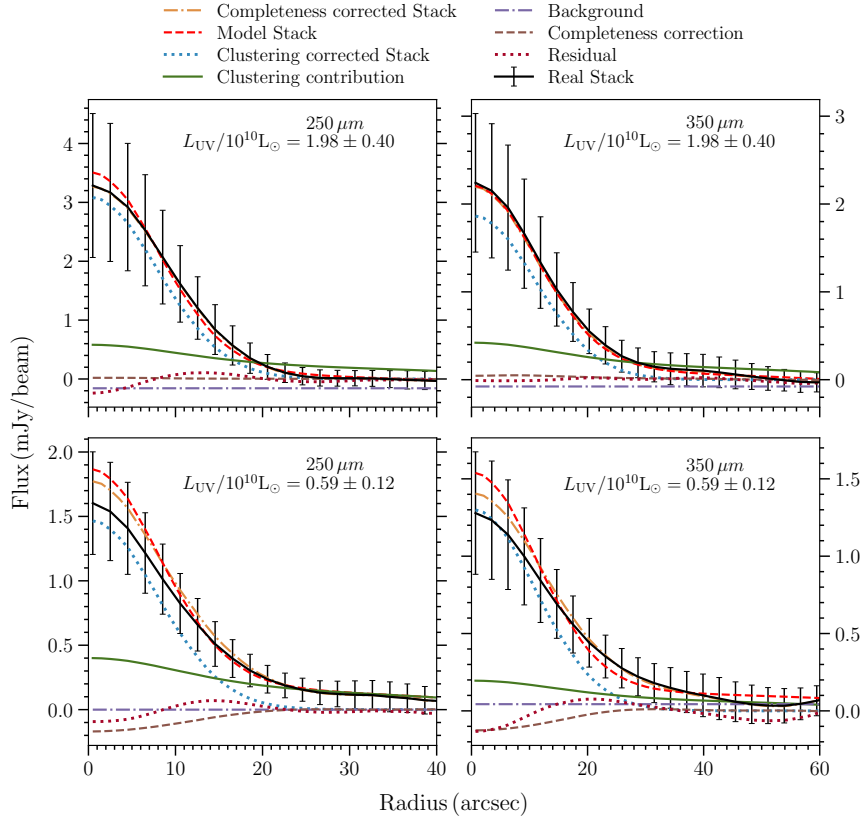


Figure 5. Here we show the radial profiles of various components in the *Herschel* SPIRE photometry described by eq. 1, by using examples of the 250 and 350 μm stacks at redshift 0.6 – 0.8 in the first and fourth luminosity bins (rows and the third and fourth columns of the left panel of Figure 4). The IR band and UV luminosity are labelled on the top right of each panel. The original stack is shown as black solid line with error bars. The stack is corrected for stacking bias and this correction is represented by brown dashed line and the yellow dot-dashed line shows the stacking bias corrected stack. The radial profile of the model fitted to the bias-corrected stack is shown by the dashed red line. We show the components of this model: the extracted flux, clustering contribution, and constant background by yellow, solid green, and dot-dashed purple, respectively. The dotted brown line represents the residual between the bias-corrected stack and its model.

During this stacking procedure, a rotation of $\pi/2$ clockwise with respect to the preceding stamp is applied to each stamp, to cancel out any potential wing-like structures of bright sources located in proximity to the stacked signal. We repeat this process for the SPIRE (250, 350 and 500 μm) and for PACS (100 and 160 μm) maps, resulting in stacked images for each FIR waveband in each UV luminosity bin. Figure 4 shows these stacked images for each FIR waveband in the redshift ranges 0.6–0.8 and 0.8–1.2, sorted according to their UV luminosities. A clear signal can be seen at the centres of most stacks.

3.2.2 Stacking bias

The stacking procedure, by its very nature, is prone to a certain degree of bias, particularly toward sources that are relatively brighter and located in regions of the sky that are less densely populated with other objects. This bias is closely related to the catalogue incompleteness (as described in Section 3 of Sharma et al. 2022). Galaxies that are either too faint to be detected or are situated in close proximity to a particularly bright source may be missed during the de-

tection process. This results in their exclusion from the final catalogue, making it incomplete. If we stack this incomplete catalogue on the FIR maps, the contribution of undetected sources to the local background of the stacks is not included.

To address this issue and recover the accurate local background of the stacks, we can use the completeness simulations from Sharma et al. (2022). These simulations involve the introduction of synthetic sources into the UVW1 image, followed by an attempt to recover them using the same detection method applied to our actual source list. The stacking of the recovered sources in the completeness simulations on the FIR maps generates correction maps to mitigate this bias. In Figure 5, we illustrate the stacking process for 250 and 350 μm maps in the first and fourth luminosity bins within the redshift range of 0.6–0.8. The corresponding radial profiles of these correction maps are depicted as brown dashed lines in Figure 5. The top panels, which represent bright UV luminosity bins at 250 and 350 μm , reveal there is not much impact of stacking bias on these bright UV bins. On the contrary, in the two bottom panels, representing faint bins, the profiles turn negative as the distance from the centre of the stack decreases, indicating a substantial bias. To

Table 2. The flux densities we obtain for the *Herschel* PACS and SPIRE bands after making the clustering correction as explained in Section 3.2. The top half of the Table corresponds to the redshift bin 0.6-0.8, and the bottom half represents the bin 0.8-1.2.

^a # sources	^b L_{FUV} ($\times 10^{10} L_{\odot}$)	$S_{100 \mu\text{m}}$ (mJy)	$S_{160 \mu\text{m}}$ (mJy)	$S_{250 \mu\text{m}}$ (mJy)	$S_{350 \mu\text{m}}$ (mJy)	$S_{500 \mu\text{m}}$ (mJy)
<i>z</i> = 0.6-0.8						
53	1.98 ± 0.40	1.96 ± 0.55	4.22 ± 0.98	3.08 ± 0.58	1.86 ± 0.49	1.05 ± 0.31
111	1.33 ± 0.27	1.44 ± 0.32	2.19 ± 0.62	1.86 ± 0.33	1.27 ± 0.26	1.04 ± 0.28
135	0.89 ± 0.17	0.94 ± 0.18	0.95 ± 0.57	1.41 ± 0.33	0.84 ± 0.27	0.34 ± 0.12
159	0.59 ± 0.12	0.72 ± 0.17	1.80 ± 0.44	1.46 ± 0.23	1.30 ± 0.22	0.70 ± 0.17
66	0.40 ± 0.08	0.61 ± 0.20	0.73 ± 0.67	1.23 ± 0.47	1.15 ± 0.39	0.61 ± 0.19
<i>z</i> = 0.8-1.2						
25	4.44 ± 0.90	0.75 ± 0.33	< 2.16	1.94 ± 0.57	1.57 ± 0.43	0.41 ± 0.36
85	2.97 ± 0.60	1.04 ± 0.24	1.81 ± 0.63	1.96 ± 0.36	1.61 ± 0.28	0.64 ± 0.23
115	1.98 ± 0.40	0.96 ± 0.25	2.54 ± 0.68	1.57 ± 0.29	1.78 ± 0.29	0.89 ± 0.23
165	1.33 ± 0.27	0.64 ± 0.18	0.98 ± 0.42	1.49 ± 0.22	0.94 ± 0.21	0.73 ± 0.17
111	0.89 ± 0.17	0.33 ± 0.19	< 0.86	0.93 ± 0.22	0.51 ± 0.27	0.32 ± 0.23
25	0.59 ± 0.12	0.44 ± 0.33	1.23 ± 0.81	0.96 ± 0.33	0.37 ± 0.24	...

^aWe ignore UV luminosity bins with < 25 sources.

^bThe bin centers of the UV LF of Sharma et al. (2022).

correct for stacking bias in the local background, these correction maps are subtracted from the stacks.

3.2.3 Stacked Photometry

The process of creating the maps using the *Herschel*-PACS and *Herschel*-SPIRE instrumentation is carried out by using various pipelines and techniques, which are independently developed and implemented by separate teams. As a result of these distinct methods, the maps produced by these instruments exhibit variations in their units and calibrations. So, in order to extract accurate flux densities from the PACS and SPIRE stacks, different approaches are employed.

The aperture photometry technique is particularly well-suited for the *Herschel*-PACS maps, as they are provided in Jy/pixel units. This technique involves measuring fluxes by using a circular aperture of a certain size to enclose the source of interest and integrate its pixel values. For the 100 μm maps, we use an aperture radius of 7.2 arcseconds, while for the 160 μm maps we use a radius of 12 arcseconds. This happens because the size of the PSF varies between the different bands and the aperture size needs to be adjusted accordingly. However, it is important to note that these extracted fluxes are not necessarily the true fluxes of the sources. To correct this, we apply corrections for the fraction of the PSF that falls outside the aperture and for any losses resulting from high-pass filtering of the data. These corrections are determined using empirical results from the PEP Data Release 1 (DR1) notes³.

The SPIRE maps are expressed in units of Jy/beam, making PSF fitting an effective method for determining the photometry of these stacks. This involves determining the flux densities of the SPIRE stacks which are equal to the peak of the PSF models fitted to the central pixels of the stacks. However, it is important to note that the SPIRE stacks can be susceptible to clustering effects, which can

result in confusion and overestimation of the stacked photometry. To mitigate this, we use a deblending approach (in Section 3) that enables us to overcome the confusion limit and minimize the clustering contribution from sources present in the prior catalogue. However, while stacking on deblended residual images reduces the flux contribution of bright off-centre sources in the prior catalogue, this method does not take into account the clustering of objects that are not part of the prior catalogue or are too faint to be detected in our residual maps. Such sources might be clustered in the IR imaging along with our UV-selected galaxies. This inherent clustering of sources can still result in an overestimation of the stacked photometry. To solve this problem, a method prescribed by Béthermin et al. (2010) is used. The method involves fitting the final stack as a linear sum of the PSF and its convolution with the angular correlation function. This is expressed mathematically as follows:

$$\mathcal{S}(\theta, \phi) + \mathcal{B} = \alpha \times \mathcal{P}(\theta, \phi) + \beta \times [\mathcal{P}(\theta, \phi) * w(\theta, \phi)]. \quad (1)$$

Here, $\mathcal{S}(\theta, \phi)$ represents the stacked stamp, $\mathcal{P}(\theta, \phi)$ represents the PSF, and $w(\theta, \phi)$ represents the angular correlation function of the galaxies under consideration. The fixed background level is represented by \mathcal{B} . The best-fit values for α , β and \mathcal{B} are found for each FIR band and UV luminosity bin, and the value of α is considered to be the final flux value for each SPIRE stack. This method provides a more comprehensive approach to account for the inherent clustering of sources and ensures more accurate photometry results.

Figure 5 shows an example of different components of this process. For this particular example, we find that clustering contributions are 18.8 and 27.3 per cent of the actual flux in the first and fourth luminosity bins for the 250 μm map. Corresponding values for the 350 map are 22.6 and 15.0 per cent. The average value of this fraction, for the 250, 350 and 500 μm maps were found to be 16, 18 and 22 per cent respectively in the redshift bin 0.6 – 0.8 and 14, 6 and 41 per cent respectively in the redshift bin 0.8 – 1.2.

³ https://www.mpe.mpg.de/resources/PEP/DR1_tarballs/readme_PEP_global.pdf

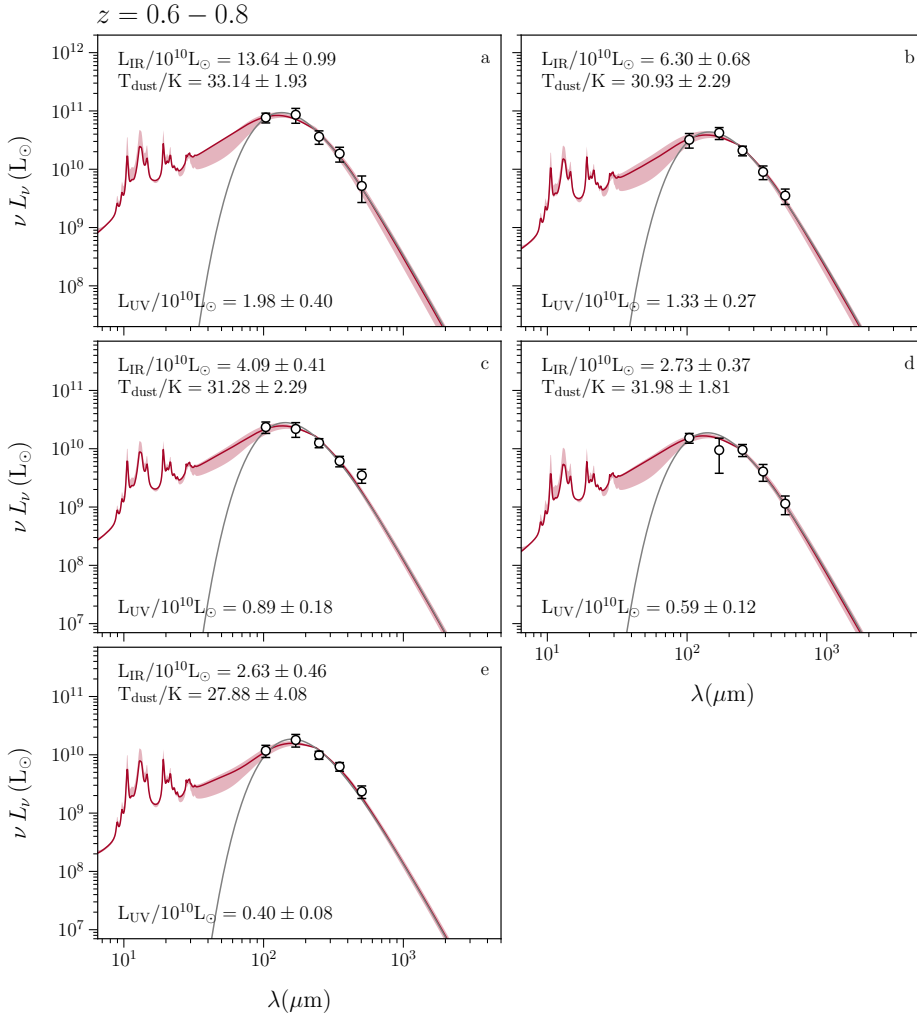


Figure 6. IR SED fits for the redshift bins $0.6 - 0.8$. Each panel represents the UV luminosity bins from brightest to faintest (from a to e). The UV luminosity of each UV LF bin is labelled at the bottom left of each panel. The black hollow circles show the FIR flux densities from *Herschel* PACS at 100 and 160 μm and *Herschel* SPIRE at 250, 350 and 500 μm . The red curve represents the best fit Boquien & Salim (2021) template to the FIR data. The shaded region represents the range of templates within $|\chi^2 - \chi^2_{\min}| \leq 1$. The grey curve is the best-fit modified black body curve. The estimates for the dust temperature and integrated IR luminosity are labelled at the top-left of each panel. Note that the IR luminosity on the x-axis is in $\nu L\nu$.

3.2.4 Errors

We use standard bootstrap to calculate the statistical errors on stacked flux densities in each bin. In each bin, N stamps are selected at random with replacement and stacked. The flux densities are calculated from these error stacks in the same fashion as the original stacks (i.e. aperture photometry for PACS and PSF photometry for SPIRE). Using 1000 bootstraps, we calculate the 68 per cent confidence intervals around the measured values. In Table 2 we show the resulting average fluxes extracted from the stacks at all FIR bands considered in this study.

3.3 IR SED fits

Now that we have obtained the stacked photometry for our galaxy sample, the next task is to extract the average IR properties from the stacked flux densities. We fit two differ-

ent types of model to the SEDs, one for determining the IR luminosity and the other for the dust temperatures.

To estimate the total IR luminosity, we fit FIR model templates to our dataset. Specifically, we utilised the two-parameter dust templates from Boquien & Salim (2021). These templates are parameterised in the total IR luminosity and specific star-formation rate, and they are built upon physically motivated dust models by Draine & Li (2007). These templates are well suited to star-forming galaxies in the luminosity range of our sample. The resulting fits are shown in Figures 6 and 7. We measure the integrated IR luminosity by integrating the rest-frame flux density from 8 to 1000 μm range, determining the fluxes, and subsequently employing the luminosity distance to calculate the IR luminosity

$$L_{8-1000\mu\text{m}} = 4\pi d_L^2(z) \int_{\nu_1}^{\nu_2} S_\nu d\nu \quad (2)$$

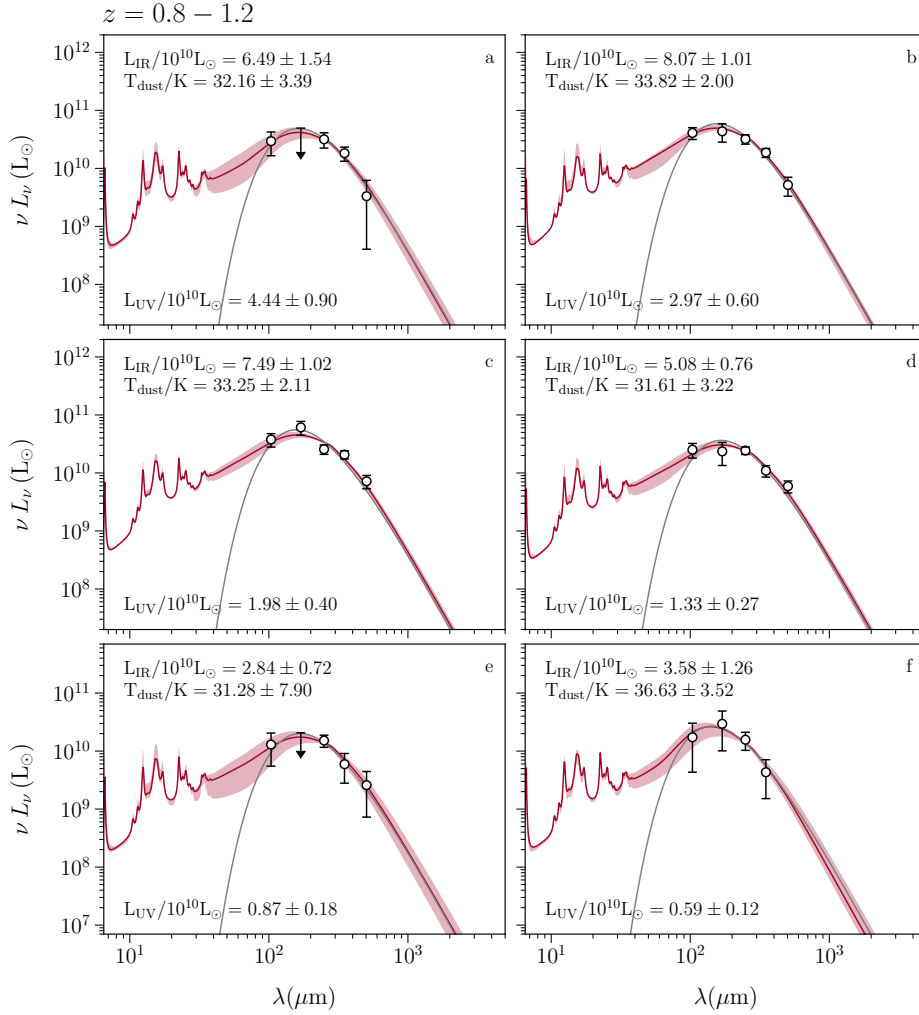


Figure 7. IR SED fits for the redshift bins $0.8 - 1.2$. Each panel represents a luminosity bin, going from the brightest to the faintest UV luminosity (a-f for $z = 0.8 - 1.2$), also labelled at the bottom-left of each panel. The colour coding is the same as in Figure 6. The dust temperature and the integrated IR luminosity are labelled in the upper left of each panel.

where ν_1 and ν_2 are the rest-frame frequencies corresponding to $8 - 1000 \mu\text{m}$ limit and d_L is the luminosity distance.

We determine the dust temperatures by fitting the isothermal grey bodies. Most of the FIR originates from large grains that radiate as isothermal grey bodies at temperatures $10 - 50 \text{ K}$ and are in equilibrium with the ambient interstellar radiation field. An isothermal black-body model can be adjusted to account for variable source emissivities and opacities, resulting in a grey-body or modified black-body model. It takes the form,

$$S(\nu) \propto \nu^\alpha B_\nu(T_d) = \frac{\nu^{\alpha+3}}{\exp\left(\frac{h\nu}{k_B T_d}\right) - 1} \quad (3)$$

for the approximation of optically thin media. Here α is the source emissivity and T_d is the characteristic dust temperature. The typical values of α fall within the range of 1.5 to 2 (Blain et al. 2003; Chapin et al. 2011; Casey et al. 2011; Viero et al. 2012) and for this work we use $\alpha = 1.5$ following Blain et al. (2003); Casey et al. (2011). We fit these grey

bodies to our stacked SEDs, with the amplitude and the dust temperature as the free parameters.

3.4 Star Formation Rate

The integrated IR luminosity calculated from the IR templates and the UV luminosity can be used to calculate obscured and un-obscured SFR respectively by using the following scaling relation (Kennicutt 1998; Murphy et al. 2011; Kennicutt & Evans 2012),

$$\log\left(\frac{\text{SFR}_{\text{FUV}}}{M_\odot \text{ yr}^{-1}}\right) = \log\left(\frac{L_{\text{FUV}}/\nu_{\text{FUV}}}{\text{ergs s}^{-1} \text{ Hz}^{-1}}\right) - 27.85 \quad (4)$$

assuming a continuous and constant SFR with the Salpeter (1955) initial mass function (IMF) over timescales longer than 10^8 yr and a mass range from 0.1 to $100 M_\odot$ and

$$\log\left(\frac{\text{SFR}_{\text{FIR}}}{M_\odot \text{ yr}^{-1}}\right) = \log\left(\frac{L_{\text{FIR}}}{\text{ergs s}^{-1}}\right) - 43.41 \quad (5)$$

assuming continuous bursts from 10 to 100 Myr, adopting the Kroupa (2001) IMF. Total SFR (SFR_{Tot}) is obtained as

Table 3. The main results of this chapter are summarised in this Table. The top and bottom halves of the Table correspond to the redshift bins 0.6-0.8 and 0.8-1.2 respectively.

^a # sources	^b L_{FUV} ($\times 10^{10} L_{\odot}$)	^c L_{FUV} ($\times 10^{10} L_{\odot}$)	^d L_{IR} ($\times 10^{10} L_{\odot}$)	^e T_{dust} (K)	^f A_{FUV} (mag)	^g SFR_{FIR} ($M_{\odot} \text{ yr}^{-1}$)	^h $\text{SFR}_{\text{FIR+FUV}}$ ($M_{\odot} \text{ yr}^{-1}$)
<i>z</i> = 0.6-0.8							
53	1.98 ± 0.40	1.95 ± 0.24	6.30 ± 0.67	30.93 ± 2.70	1.15 ± 0.39	9.42 ± 1.00	15.18 ± 2.33
111	1.33 ± 0.27	1.31 ± 0.15	4.09 ± 0.42	31.28 ± 2.20	1.13 ± 0.38	6.11 ± 0.64	9.97 ± 1.54
135	0.89 ± 0.17	0.89 ± 0.10	2.73 ± 0.35	31.98 ± 1.79	1.13 ± 0.39	4.08 ± 0.52	6.66 ± 1.07
159	0.59 ± 0.12	0.60 ± 0.07	2.63 ± 0.44	27.88 ± 3.68	1.39 ± 0.57	3.87 ± 0.66	5.59 ± 0.91
66	0.40 ± 0.08	0.41 ± 0.04	2.14 ± 0.65	27.04 ± 4.13	1.53 ± 0.84	3.08 ± 0.97	4.23 ± 1.06
<i>z</i> = 0.8-1.2							
25	4.44 ± 0.90	4.43 ± 0.58	6.49 ± 1.54	32.16 ± 3.39	0.68 ± 0.26	9.71 ± 2.30	22.60 ± 5.23
85	2.97 ± 0.60	2.92 ± 0.31	8.07 ± 1.01	33.82 ± 2.00	1.04 ± 0.35	12.07 ± 1.50	20.69 ± 3.49
115	1.98 ± 0.40	2.02 ± 0.21	7.49 ± 1.02	33.25 ± 2.11	1.28 ± 0.47	11.20 ± 1.52	16.96 ± 2.60
165	1.33 ± 0.27	1.33 ± 0.16	5.08 ± 0.76	31.61 ± 3.22	1.29 ± 0.49	7.60 ± 1.13	11.45 ± 1.81
111	0.89 ± 0.17	0.92 ± 0.10	2.84 ± 0.72	31.28 ± 7.09	1.16 ± 0.52	4.25 ± 1.07	6.82 ± 1.42
25	0.59 ± 0.12	0.64 ± 0.05	3.58 ± 1.26	36.63 ± 3.52	1.66 ± 0.98	5.36 ± 1.88	7.07 ± 1.98

^aThis column shows the number of sources in each UV luminosity bin. UV LF bins with < 25 sources have been ignored.

^bThe bin centers of the UV LF in [Sharma et al. \(2022\)](#). These values are used as labels in this work.

^cMean of the UV luminosity of the sources inside the UV LF bins. We use these values for all the calculations in this paper.

^dAverage integrated IR luminosity obtained from the stacked flux densities.

^eAverage dust temperature of galaxies in each UV LF bin, obtained from the MBB fits.

^fAverage dust attenuation from eq. 6.

^gThe SFR estimated from the IR luminosity.

^hThe total SFR, calculated as the sum of the IR and UV components.

the sum of the contributions from the luminosities of FIR (SFR_{FIR}) and FUV (SFR_{FUV}). The SFR_{FUV} value based on the [Salpeter \(1955\)](#) IMF is transformed into the equivalent value corresponding to the [Kroupa \(2001\)](#) IMF through a multiplication by a factor of 1.8.

3.5 Dust Attenuation

Using the IR and UV luminosities, we calculate the IRX ([Meurer et al. 1999](#)), such that $\text{IRX} = L_{\text{IR}}/L_{\text{UV}}$. Different relations are used in the literature ([Meurer et al. 1999](#); [Seibert et al. 2005](#); [Hao et al. 2011](#); [Nordon et al. 2013](#)) to convert the IRX ratio into the dust attenuation in the UV luminosity. For the sake of comparison, we apply the relation commonly used in previous studies (e.g. [Nordon et al. 2013](#); [Heinis et al. 2013](#); [Álvarez-Márquez et al. 2016](#)),

$$A_{\text{FUV}} = 2.5 \log (1 + 0.59 \times \text{IRX}). \quad (6)$$

This can be used to correct for the UV light absorbed by the dust and calculate the total SFR in the next Section. In order to make this correction to the unobscured SFR we use the relation from [Nordon et al. \(2013\)](#) given by

$$\log(\text{SFR}_{\text{Tot}}) = \log(\text{SFR}_{\text{FUV}}) + 0.4 \times A_{\text{FUV}} \quad (7)$$

4 RESULTS

We stack maps of FIR emission obtained from *Herschel* on ultraviolet (UV) selected sources that lie in the redshift range of 0.6 to 1.2. To determine the average stacked photometry in the FIR for these sources, we fit the IR model templates from [Boquien & Salim \(2021\)](#) and integrating the results over the wavelength range of 8 to 1000 μm . The results indicate that the typical IR luminosities of the stacked

galaxies fall within the range of $2.15 \times 10^{10} L_{\odot}$ to $6.30 \times 10^{10} L_{\odot}$ at redshift 0.7 and $3.58 \times 10^{10} L_{\odot}$ to $6.49 \times 10^{10} L_{\odot}$ at redshift 1.0. On average, our sample is composed of galaxies belonging to the normal (sub-luminous; $L_{\text{IR}} < 10^{11} L_{\odot}$) infrared galaxies.

In order to obtain the average dust temperatures, we fit isothermal grey bodies to the average FIR photometry in each UV luminosity bin. These temperatures are presented in the left panel of Figure 8 as functions of IR luminosity. Additionally, we have plotted the luminosity-weighted dust temperatures as a function of redshift in the middle panel of Figure 8, along with literature values for comparison. Individual temperatures, calculated in the UV Luminosity Function (UV LF) bins, are shown as a function of UV luminosity in the right panel of Figure 8.

Using the estimated FIR luminosities, we calculated the IRX in each UV luminosity bin. In Figure 9, we have plotted the average value of IRX as a function of the redshift. IRX as a function of the FIR and FUV luminosities are plotted in Figures 10 and 11, respectively. The top panel of Figure 11 also shows the UV LF from [Sharma et al. \(2022\)](#). This dust attenuation (A_{FUV}) in the UV radiation is parametrised in terms of the IRX ratio, as described by eq. 6, and labelled as the secondary y-axis on the right-hand side of the panels in Figures 9 and 10. We estimate the SFR of our galaxies in Section 3.4, and present the results in Figure 12 comparing the estimates from the UV and IR luminosities as well as the total SFR. Then in Figure 13, we show IRX as a function of the total SFR.

Finally, we use these values of A_{FUV} to correct the SFR density (SFRD), which is calculated from dust-attenuated UV radiation. The SFRD is estimated from the luminosity density estimates, as explained in Section 3.4, where the estimates of luminosity density calculated using rest-frame UV radiation come from [Sharma et al. \(2022\)](#). In Figure 14,

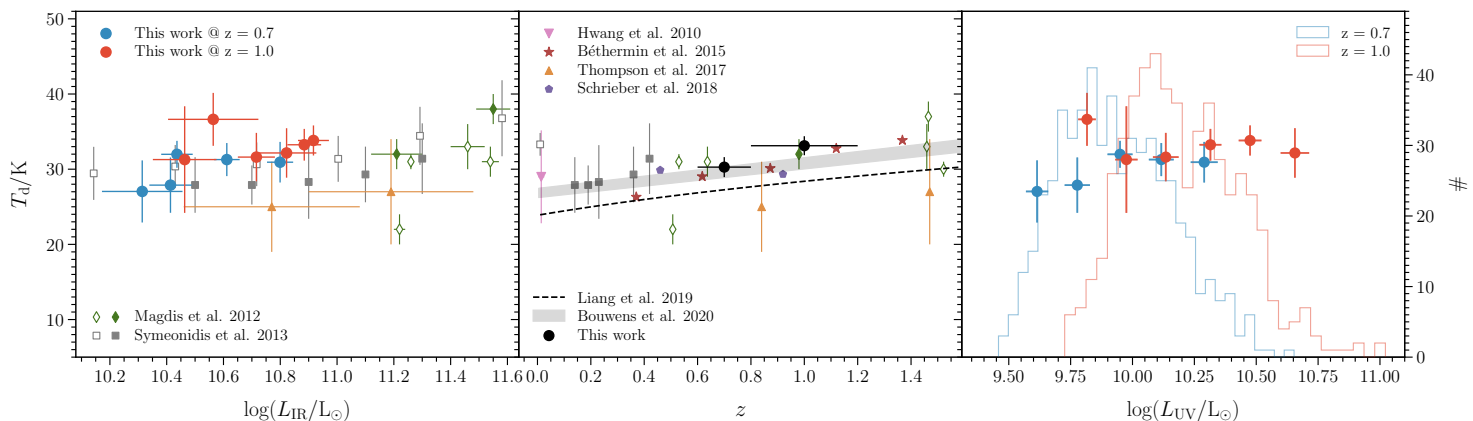


Figure 8. Dust temperature as a function of total IR luminosity, redshift and UV luminosity. *Left panel:* dust temperature in logarithmic IR luminosity bins. The results from this work at redshift bins centred at 0.7 and 1.0 are shown in blue and red circles, respectively. For comparison, we also plot the literature results from Magdis et al. (2012) as green diamond symbols. The solid and hollow symbols represent the values from stacking analysis and individual star-forming galaxies, respectively. The grey squares represent the median temperatures of the IR-selected galaxies from Symeonidis et al. (2013). The hollow squares represent the values for the galaxies in their local sample ($z < 0.1$). The yellow triangles represent the results for the H_{α} selected samples from Thomson et al. (2017). *Middle panel:* average temperature as a function of redshift. The solid circles in black show the values obtained in this work by luminosity weighing the temperatures in redshift bins centred at 0.7 and 1.0. We show the redshift weighted mean dust temperature of the galaxies in the local Universe from Hwang et al. (2010) as a pink downward triangle. The brown stars and purple pentagons represent the estimates of Béthermin et al. (2015) and Schreiber et al. (2018). These values are taken from the compilation of Bouwens et al. (2020). The grey shaded area shows the fit from Bouwens et al. (2020). The dashed black line is the predicted trend for the $T_d - z$ relation from Liang et al. (2019). *Right panel:* dust temperature of the grey body fits as a function of UV luminosity. The blue and red histograms represent the distributions of the star-forming galaxies in the UV luminosity space for redshift bins centred at 0.7 and 1.0 respectively. The y-axis on the right represents the number of sources. The data points share the redshift colour scheme with the histograms.

we present the estimates for the total SFRD after it has been corrected for dust attenuation, providing a more accurate picture of the star formation activity in these galaxies.

5 DISCUSSION

The aim of this paper is to study the dust properties of UV-selected galaxies in the redshift range of 0.6-1.2. The galaxies selected through the UVW1 filter on XMM-OM are stacked on the FIR imaging from *Herschel* PACS and SPIRE instruments, and the dust properties are constrained in UV luminosity bins of the UV LF in the same redshift range. We considered only luminosity bins with at least 25 sources in each redshift bin (at 0.7 and 1.0), to obtain robust statistics.

5.1 Dust Temperature and Infrared Luminosities

We start with the dust temperature and total IR luminosities of galaxies and explore their correlation if any. The relationship between dust temperature and IR luminosity is related to the physical conditions within star-forming regions, from which the IR emission originates. In this context, higher temperatures indicate either more compact or more luminous star-forming regions. The equilibrium temperature essentially depends on the UV flux that impinges on the dust grains. A correlation between dust temperature and IR luminosity has been observed in some previous studies (e.g. Soifer et al. 1987; Dunne et al. 2000; Dale et al. 2001; Chapman et al. 2003; Symeonidis et al. 2009; Magnelli et al.

2014) and is suggested to be likely the result of the transition of galaxies into starburst phase (Magnelli et al. 2014).

In our study, we use the isothermal graybody and IR model templates to fit the stacked *Herschel* PACS and SPIRE photometry, allowing us to calculate the dust temperature and IR luminosities. Our results are directly comparable to other studies in the literature that have adopted similar definitions of dust temperature and used MBBs for calculations. However, if a different definition or technique is used, it will be specifically noted. Our findings do not suggest any significant trend in dust temperature with IR luminosity for a fixed redshift (as seen in the left panel of Figure 8).

If averaged over the UV LF bins, the average temperature increases very slightly with redshift within the range explored in this study. However, the difference is not very significant and the values are within the 2σ distance. The range of redshifts explored in this work is not wide enough to make any conclusive remarks, so we include measurements at other redshifts from previous studies (from redshift 0.15-1.5; Magdis et al. 2012; Symeonidis et al. 2013; Béthermin et al. 2015; Thomson et al. 2017; Schreiber et al. 2018). In this case, now we observe a weak trend, which is also confirmed by the fit from Bouwens et al. (2020). The fit is mainly driven by values from Béthermin et al. (2015) and Schreiber et al. (2018), but as we can see (middle panel of Figure 8) it is also somewhat consistent with other works considered in our study. Our values seem to be in agreement with these previous studies and the fit from Bouwens et al. (2020). In the same plot, we show the trend found by Liang et al. (2019) for galaxies at redshifts 2 and higher, extrapolated to redshift

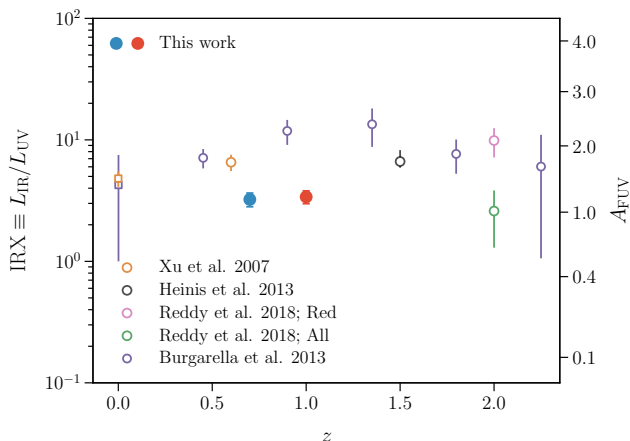


Figure 9. Here we show the IRX ratio as a function of redshift. On the right side of the panel, we plot the attenuation A_{FUV} in the UV radiation due to dust, which is parameterised as a function of the IRX. The blue and red solid circles show the values obtained in this work. The hollow circular symbols represent the literature estimates from Xu et al. (2007), Heinis et al. (2013), Reddy et al. (2018) and Burgarella et al. (2013) in yellow, black, green and purple colours respectively. The pink hollow circles represent the subset of Reddy et al. (2018) sample, referred to as “Red” galaxies. The redshift 0 data from Xu et al. (2007) and Burgarella et al. (2013).

0.01. This trend is offset towards lower temperatures from the values obtained in this and previous works. We compare our results with the values of dust temperature calculated by Hwang et al. (2010) and Symeonidis et al. (2013) for their samples of IR galaxies. About 90 per cent of Hwang et al. (2010) galaxies have $\log(L_{\text{IR}}/L_{\odot}) \leq 11.2$, which is roughly the upper limit of the highest IR luminosity bin. They estimated the median dust temperature to be 28.98 K, with a 16–84th percentile range of 24.78 K to 37.13 K. These values as a function of the median redshift of the galaxies are plotted in the middle panel of Figure 8 along with the mean dust temperature for the Symeonidis et al. (2013) local sample. On comparison, it can be seen that the average dust temperature does not evolve significantly from redshift 1 to the present time.

Despite much effort, determining the precise relationship between dust temperature and redshift is a difficult task, especially in light of recent results, which often appear contradictory. Some studies observe that the dust temperature increases from the local Universe to high redshifts (e.g. Magdis et al. 2012; Magnelli et al. 2014; Béthermin et al. 2015; Schreiber et al. 2018). Conversely, others argue for a colder dust temperature at higher redshifts (e.g. Chapman et al. 2002; Hwang et al. 2010; Symeonidis et al. 2009, 2013; Kirkpatrick et al. 2012, 2017). There is a third group of studies that find no compelling evidence for a redshift-dependent evolution of dust temperature (e.g. Casey et al. 2018; Drew & Casey 2022). These conflicting outcomes can be partly attributed to selection bias in flux-limited samples (Liang et al. 2019), as well as to the influence of various factors capable of significantly affecting dust temperature. These factors include, but are not limited to, the specific SFR (Magnelli et al. 2014), the amount and opacity of dust, the gas

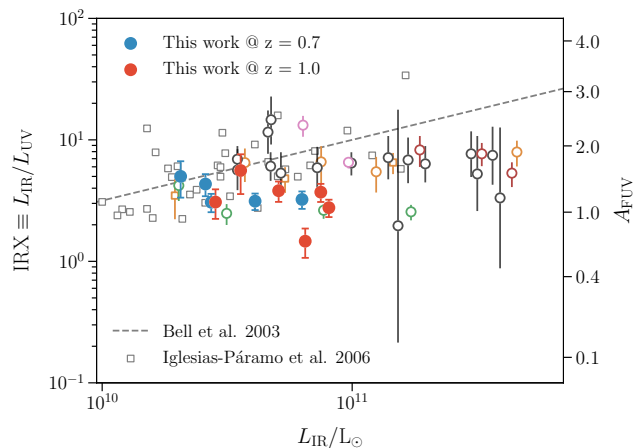


Figure 10. We plot the IRX ratio as a function of FIR luminosity in this Figure. The symbols and colour coding is the same as in Figure 9. We plot the individual galaxies in the nearby Universe, from the NUV selected sample (with a median redshift of 0.013) from Iglesias-Páramo et al. (2006) as grey hollow squares, in addition to other literature values mentioned in Figure 9.

metallicities etc. (Liang et al. 2019). In fact, the correlation between dust temperature and specific SFR is suggested to be more robust and statistically significant than that with redshift (Magnelli et al. 2014; Schreiber et al. 2018). Our results for the UV-selected galaxies agree with the findings of the third group of studies mentioned above. However, we remark here that all of these studies are conducted on IR-selected galaxies samples.

The dust temperature and UV luminosity, are plotted in the right panel of Figure 8. From the plot we observe a modest correlation between these two parameters only for redshift 0.7. The Spearman correlation coefficients for these variables are 0.60 and -0.03, at redshifts of 0.7 and 1.0; however, the significance for any correlations is very low.

5.2 Dust Attenuation

The IRX, which is a ratio of total IR to UV luminosity, is commonly used to estimate the amount of dust attenuation of UV light. We calculated the median dust attenuation values to be 1.15 and 1.22 magnitudes (equivalent to IRX of 3.17 and 3.49) in the redshifts bins centered at 0.7 and 1.0 respectively. These values suggest that the dust content of our galaxies does not change significantly over this redshift range.

As depicted in Figure 9, the average dust attenuation appears to remain constant from the local Universe up to a redshift of 2.5 (Xu et al. 2007; Heinis et al. 2013; Burgarella et al. 2013). We note here that Xu et al. (2007) used 24 μm data to estimate their average dust attenuation, while Burgarella et al. (2013) used the 60 μm LF of Takeuchi et al. (2005) for their $z = 0$ estimates. Our results at redshifts of 0.7 and 1.0 are offset below other work at similar redshifts (Xu et al. 2007; Burgarella et al. 2013), but are in good agreement with studies in the local Universe (Burgarella et al. 2013) or redshifts higher than those explored in our study (Burgarella et al. 2013; Reddy et al. 2018).

We do observe a weak trend between the dust attenuation and the total IR luminosity for our UV-selected galaxies in the redshift range 0.6 – 1.2 (Figure 10), wherein the dust attenuation decreases with IR luminosity at redshifts 0.7 and 1.0. The correlation coefficients are -0.61 and -0.43. However, these correlations have low significance (p values of 0.28 and 0.36 at $z = 0.7$ and 1.0), and the range of IR luminosities of our galaxies is not wide enough to draw any definitive conclusions.

Previous studies at redshifts ranging from 0.6 to 3 do not report any trends with IR luminosity (Xu et al. 2007; Heinis et al. 2013; Álvarez-Márquez et al. 2016; Reddy et al. 2018). In Figure 10, we plot the NUV-selected galaxies from *GALEX* surveys in the local Universe of Iglesias-Páramo et al. (2006), who used the *IRAS* 60 μm data to estimate L_{IR} . Their galaxies follow a relation (grey dashed line in Figure 10), obtained by Bell (2003) for a local compilation which contains sources from the literature with FUV, optical, IR (60 and 100 μm) and radio wavelengths. The local galaxies thus show a correlation wherein galaxies with high IR luminosity are more dust attenuated, which is expected as the increased dust attenuation results in a larger fraction of UV radiation being absorbed by dust, consequently leading to a higher IR luminosity. It is interesting why this behaviour stops as we go past redshift 0.6. The majority of galaxies in the local datasets described in Iglesias-Páramo et al. (2006) and Bell (2003) do not appear to exceed a luminosity of $2 \times 10^{11} L_{\odot}$. Below this IR luminosity, the results from the local samples of Bell (2003), Iglesias-Páramo et al. (2006), and the high redshift values from the literature are consistent. However, above this limit, there seems to be a noticeable discrepancy. The discrepancy may imply that the Bell (2003) relation does not apply beyond the luminosity range of local galaxies from which it was derived, although it is also possible that the relationship between IRX and IR luminosity may change with redshift. The range of IR luminosities in our sample closely resembles that of the local datasets. However, our findings align with local results only at IR luminosities below $5 \times 10^{10} L_{\odot}$. As luminosity increases, our results begin to deviate from the Bell (2003) curve and other high redshift measurements.

In Figure 11, we present the relationship between IRX and UV luminosity. We observe a trend in both redshift ranges for IRX to be smaller at higher luminosities. The Spearman correlation coefficients are -0.6 and -0.8 (with p-values of 0.28 and 0.04) at redshifts of 0.7 and 1.0.

In the existing literature, various studies have proposed different behaviours. There are studies using UV selection from the local Universe up to redshift 8, which report a decreasing trend of IRX with increasing L_{UV} (e.g. Buat et al. 2009; Bouwens et al. 2009; Kurczynski et al. 2014). Some others report a flat IRX – L_{UV} relationship for UV-selected galaxies with average redshifts in the range 0.6 – 2 (e.g. see Xu et al. 2007; Heinis et al. 2013) and for Lyman-break galaxies with average redshifts from 2 to 8 (see Wilkins et al. 2011; Bouwens et al. 2012; Álvarez-Márquez et al. 2016; Reddy et al. 2018). We remark here that Bouwens et al. (2009, 2012), Wilkins et al. (2011), and Kurczynski et al. (2014), used the UV spectral slope to estimate dust attenuation, and the results of Buat et al. (2009) were based on rather uncertain mid-IR to total-IR calibrations.

Our average IRX values within the two redshift bins

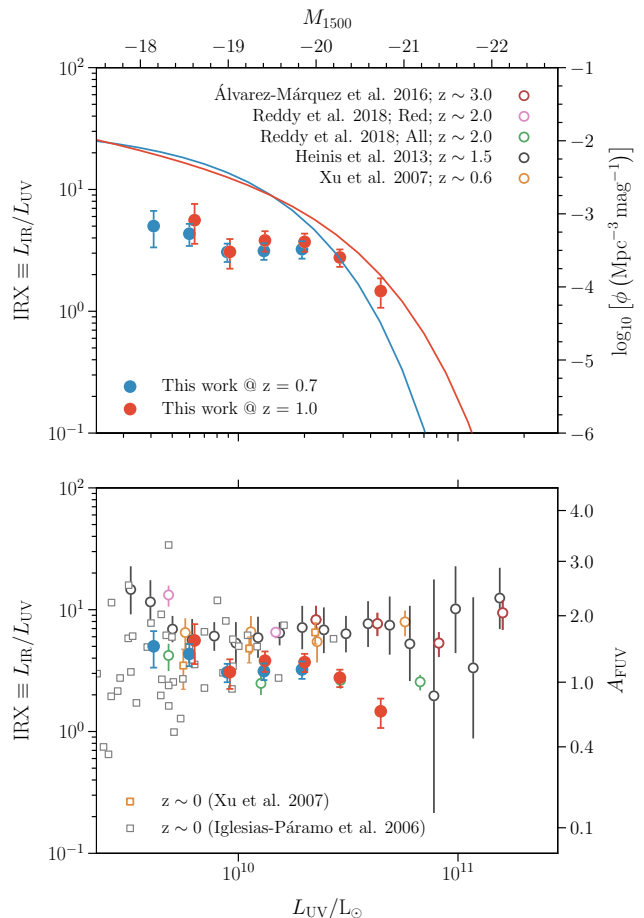


Figure 11. The IRX ratio as a function of UV luminosity. In the *top panel* we show the values calculated in our study as blue and red solid circles at redshifts 0.7 and 1.0. We also show the UV luminosity functions of galaxies at redshifts of 0.7 (blue) and 1.0 (red) from Sharma et al. (2022) with the corresponding y-axis label on the right hand side. Note that the y-axes of the IRX values (datapoints) and the luminosity functions (curves) are independent of each other. The *bottom panel* shows our IRX values along with the results from the literature. The symbols and colour coding is the same as in Figures 9 and 10.

(0.6 – 0.8 and 0.8 – 1.2) are lower than those reported in previous stacking studies conducted at different redshifts, specifically $z = 0.6$ (Xu et al. 2007), $z = 1.5$ (Heinis et al. 2013) and $z = 3.0$ (Álvarez-Márquez et al. 2016). Furthermore, comparing to the results of Xu et al. (2007), who stacked the local ($z = 0$) UV-selected sample of Iglesias-Páramo et al. (2006), we observe that their average IRX value is also higher than what we find in both our redshift bins (Figures 10 and 11). A similar observation was made by Reddy et al. (2018), using a sample that is dominated by blue ($\beta \leq -1.4$) star-forming galaxies at redshift ~ 2 . Our average results at redshifts 0.7 and 1.0 tend to align more closely with the values reported by Reddy et al. (2018) than the other studies.

The discrepancies in the behaviour of the IRX – L_{UV} relation are often attributed to the way samples are selected (Buat et al. 2007a). UV-selected samples, in particular, tend to favour galaxies with lower dust content, result-

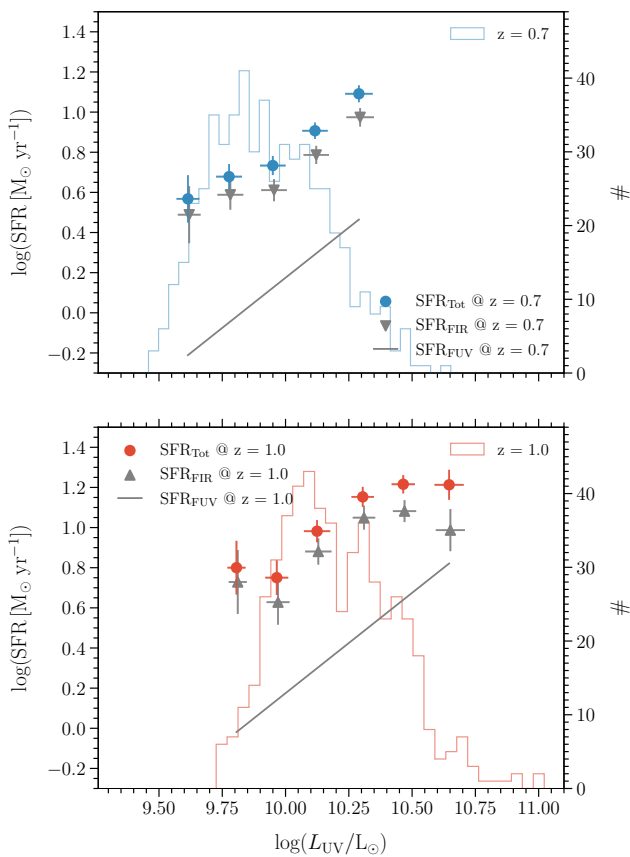


Figure 12. We plot the SFR as a function of the UV luminosity at redshifts 0.7 and 1.0 respectively in the *top* and *bottom* panels of this Figure. The histograms represent the distributions of the star-forming galaxies in the UV luminosity space with the number of galaxies marked on the y-axis on the right axis similar to the right panel of Figure 8. The blue and red-filled circles show the total SFR at redshifts 0.7 and 1.0. The gray-filled triangles show the SFR from IR luminosity and the lines show the SFR calculated using the UV luminosity.

ing in most bright UV galaxies having low IR luminosities. Consequently, IRX is expected to exhibit a negative correlation with L_{UV} for a UV-selected sample. For our case, the downward trend can be explained if we assume a population of star-forming galaxies and a distribution of extinction in those galaxies. We would expect the lowest extinction galaxies to have the largest contribution in the brightest absolute magnitude bins, so that the balance of absorbed sources, or the typical degree of extinction, will change as we move from the bright end to the faint end of the LF.

5.3 Total star formation rate

We estimate the SFR for our UV-selected sample using equations in Section 3.4. The resulting values of the total SFR, which is the sum of the UV and infrared components of the SFR ($SFR_{Tot} = SFR_{UV} + SFR_{IR}$), are shown in Figure 12 assuming the Kroupa (2001) IMF. For comparison, we have also plotted the SFR values that were calculated using the UV luminosity (SFR_{UV}) and the IR luminosity (SFR_{IR}) separately.

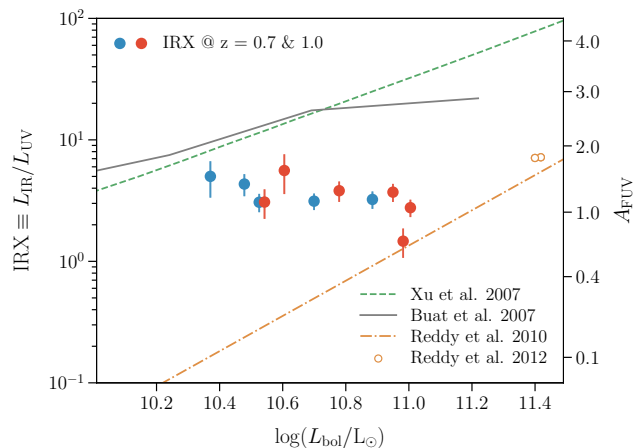


Figure 13. We plot here the IRX ratio and the dust attenuation (A_{FUV}) as a function of the bolometric luminosity (which is used as a proxy for the total SFR by the studies, we compare our results to). The red and blue solid circles represent our values at redshift 0.6 – 0.8 and 0.8 – 1.2. The green dashed line, grey solid line and yellow dot-dashed line show the results from Xu et al. (2007); Buat et al. (2007b) and Reddy et al. (2010). The yellow hollow circles represent the values of average dust attenuation from Reddy et al. (2012).

It is evident from Figure 12 that if we relied solely on ultraviolet (UV) indicators, we would be underestimating the mean SFR by approximately a factor of 3 in redshift bins centred at 0.7 and 1.0, respectively. At redshift 0.7, the underestimate decreases as the UV luminosity increases. This is expected behaviour, as we observe the same in the IRX vs L_{UV} plot (Figure 11).

The difference between the UV-derived and total SFR is indicative of the substantial amount of dust present, which attenuates the UV light, thereby obscuring the star formation. The relationship between this attenuation and the SFR should be worth investigating. Some previous studies using samples selected using the UV (Buat et al. 2007b; Reddy et al. 2010, 2012), the Lyman-break (Reddy et al. 2006) and 24 μm observation (Zheng et al. 2007) have demonstrated a positive correlation between these two quantities i.e. higher dust attenuation for higher SFR (or bolometric luminosity). However, we did not find a significant correlation between these quantities in either redshift bin in this study: in Figure 13, apart from a single low datapoint, IRX appears roughly constant with bolometric luminosity. We also show results from UV-selected galaxies in the local Universe (Buat et al. 2007b), at redshift of 0.6 (Xu et al. 2007) and at redshift of 2 (Reddy et al. 2012). For comparison, the values for Lyman- α galaxies at redshift 2 (Reddy et al. 2010) are also plotted. We can see that the Buat et al. (2007b) findings also have a flat trend in the luminosity range of our sources, although their values have higher normalisation. Among the redshift bins of our study (0.6 – 0.8 and 0.8 – 1.2) we did not observe any significant change in dust attenuation given the bolometric luminosity.

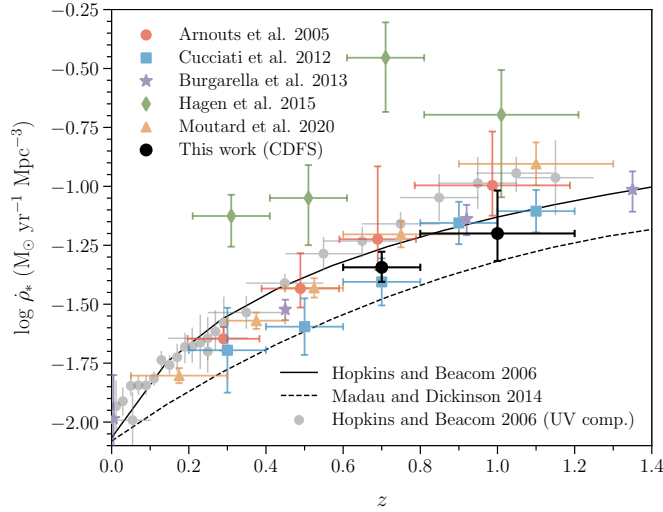


Figure 14. The SFRD of the UV-selected star-forming galaxy sample. Our results are presented as black solid circles. We plot the literature results as blue squares (Cucciati et al. 2012), purple stars (Burgarella et al. 2013), green diamonds (Hagen et al. 2015) and yellow triangles showing Moutard et al. (2020) values corrected for dust attenuation using Le Flocc’h et al. (2005). The grey circles represent dust-corrected UV-based SFRD from the Hopkins & Beacom (2006) compilation. From this compilation, we plot the SFRD values calculated using the Arnouts et al. (2005) data in red circles. Trends obtained from Hopkins & Beacom (2006) and Madau & Dickinson (2014) are shown as solid black and dashed lines, respectively.

5.4 The star formation rate density

We calculate the contribution to the SFRD at redshift 0.7 and 1.0 from the UV sources using our UV-selected galaxy sample. To estimate the SFRD, we use the UV luminosity density provided by Sharma et al. (2022) at these redshifts, which is then converted into the SFRD using eq. 4, assuming the Kroupa (2001) IMF. We take into account the impact of dust on the UV estimates and correct them accordingly by using the dust attenuation inferred from the IRX ratio (see Eq. 6 in Section 3.5).

Our results are illustrated in Figure 14 along with previous estimates based on UV luminosity. We do not find any significant evolution of the SFRD from redshift 1.0 to 0.7. Compared to previous works such as Arnouts et al. (2005) and other UV luminosity-based estimates compiled in Hopkins & Beacom (2006), we observe a good level of agreement at redshifts 0.7 and 1.0. It is worth noting that this fit is primarily driven by a large number of data points at redshifts smaller than 0.5, covers a wider range of redshifts, and takes into consideration the SFRD measured from tracers other than UV. At redshift 0.7, we notice a deviation of more than 1σ from the UV compilation of Hopkins & Beacom (2006) and Moutard et al. (2020). However, our results are within the error bars of the SFRD calculated using the Arnouts et al. (2005) results.

We calculate the fraction of obscured star formation, using the obscured to total star formation ratio, assuming the energy balance argument. These are estimated to be 65 and 68 per cent at redshifts 0.7 and 1.0, suggesting the dominance of dust-obscured components in the overall SFRD in these redshift bins. These figures also imply that the dust content of our galaxies does not change significantly over this redshift range. Contrasting these results with those from the local Universe - roughly 75 per cent dust obscured star formation obtained by Magnelli et al. (2013), it is evident

Table 4. The luminosity and SFR density of the UV-selected galaxies from CDFS at redshifts 0.7 and 1.0.

$a(z)$	$b \log \rho$ ($\text{erg s}^{-1} \text{Hz}^{-1} \text{Mpc}^{-3}$)	$c A_{\text{FUV}}$ (mag)	$d \log \rho_*^{\text{UV}}$ ($\text{M}_\odot \text{yr}^{-1} \text{Mpc}^{-3}$)	$e \log \rho_*^{\text{corr}}$
0.7	$26.31^{+0.07}_{-0.06}$	1.75	$-1.80^{+0.07}_{-0.06}$	$-1.34^{+0.07}_{-0.06}$
1.0	$26.43^{+0.18}_{-0.12}$	1.70	$-1.68^{+0.18}_{-0.12}$	$-1.19^{+0.18}_{-0.12}$

^aThe center of the redshift bin.

^bFrom Sharma et al. (2022).

^cThe median value for all UV luminosity bins.

^dUn-obscured SFRD Calculated from the UV luminosity density using the Kennicutt (1998) calibration assuming the Kroupa (2001) IMF.

^eThe un-obscured SFRD corrected for the dust attenuation using A_{FUV} .

that there is no significant evolution in the fraction of dust-obscured star formation rate density from redshift 0 to 0.7, and even further to redshift 1 (Le Flocc’h et al. 2005).

The results presented above may not accurately reflect the total star formation activity in the studied redshift range because of the possibility of missing heavily obscured systems in our UV selection. It has previously been shown that these particular galaxies, (U)LIRGs, dominate star formation activity in the redshift range explored in our study (Le Flocc’h et al. 2005). So, we test whether or not the contribution from bright IR galaxies (which might not have been detected in our UV-selected catalogue) makes a significant difference to the SFRD estimated in this study. To estimate the SFRD of these bright IR galaxies, we used the results from Le Flocc’h et al. (2005) and Magnelli et al. (2013). The study conducted by Le Flocc’h et al. (2005) utilised a sample of 24 μm sources from *Spitzer* MIPS in CDFS to determine the IR luminosity function and the total IR luminosity density at redshift $0 \leq z \leq 1$. On the other hand, Magnelli et al. (2013)

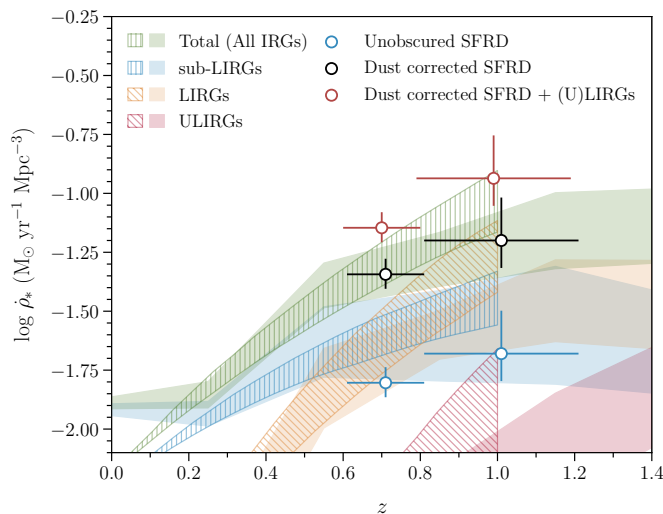


Figure 15. We compare our results for the SFRD with and without dust correction. For reference, we also plot the total SFRD calculated from the IR galaxies from the studies by [Le Flocc’h et al. \(2005\)](#) and [Magnelli et al. \(2013\)](#) as hatched and shaded regions, respectively. These works also considered the contributions of normal IR galaxies (sub-LIRGs), LIRGs, and ULIRGs to the total IR luminosity density (and SFRD). Here, we show the total SFRD from the IR galaxies as green-coloured regions. Contributions from sub-LIRGs, LIRGs, and ULIRGs are shown as blue, yellow, and red regions. The data points show the values obtained in this work. The blue hollow circles represent the unobscured SFRD obtained from the UV luminosity density of [Sharma et al. \(2022\)](#) without correcting for dust attenuation. The black hollow circles are the dust-corrected values using the attenuation factor (A_{FUV}) calculated as shown in Section 3.5. The red hollow circles represent the SFRD obtained if we add the contribution of the (U)LIRGs from the studies mentioned above to the dust-corrected UV SFRD (black circles).

used observations of GOODS fields from *Herschel* PACS to obtain the IR LF and luminosity density. Both of these studies also provide insight into the relative contribution of Luminous Infrared Galaxies (LIRGs; $10^{11}L_{\odot} < L_{IR} < 10^{12}L_{\odot}$; see [Sanders & Mirabel \(1996\)](#), Ultra-Luminous Infrared Galaxies (ULIRGs; $10^{12}L_{\odot} < L_{IR} < 10^{13}L_{\odot}$; [Sanders & Mirabel \(1996\)](#); [Genzel et al. \(1998\)](#)), and the normal (sub-luminous; $L_{IR} < 10^{11}L_{\odot}$) infrared galaxies. A summary of their findings is depicted in Figure 15, which shows reasonable consistency up to redshift 0.6. However, as we move towards redshift 1, the values obtained by [Le Flocc’h et al. \(2005\)](#) start to deviate slightly above the ones from [Magnelli et al. \(2013\)](#). It is important to note here that neither of these studies are corrected for the contribution of the AGN to the IR galaxies, and AGN are known to have a significant effect on the IR luminosity of galaxies from local Universe up to a redshift 2.5 ([Symeonidis & Page 2019, 2021](#)).

We compare the values estimated in our study to the average of these two works in Figure 15. The blue circles show our unobscured SFRD calculated from direct UV observations. It is noteworthy that these values are observed to fall on the blue-shaded regions, which represent the contribution of sub-LIRGs to the overall IR contribution. This indicates that our sample may account, to some extent, for the contribution from these sub-LIRGs observed in the $24 \mu\text{m}$ and FIR samples of [Le Flocc’h et al. \(2005\)](#) and [Magnelli et al. \(2013\)](#), respectively. This behaviour is somewhat expected, as the IR luminosities of the majority of our UV-selected galaxies fall within the range, which is typically associated with the sub-LIRG population. Thus, the sub-LIRG populations might receive some contribution to the SFRD from the UV-bright sources. The black hollow circles in Figure 15 show the dust-corrected SFRD values. These values are

generally consistent with the total IR SFRD estimates of [Le Flocc’h et al. \(2005\)](#) and [Magnelli et al. \(2013\)](#). We added the average of the (U)LIRGs SFRD from these studies to our dust-corrected UV SFRD measurements. This yields values (red circles in Figure 15) that greatly exceed the total IR luminosity density (and the dust-corrected UV SFRD estimates). This is an interesting outcome, suggesting that if we consider (U)LIRGs as a distinct population from our UV galaxies and sum their SFRD values to our dust-corrected UV SFRD, we arrive at a value much higher than if we were to correct the UV SFRD for dust extinction using a mean attenuation correction. This implies that although these populations (ULIRGs and LIRGs) might not be represented in our sample, we have not missed much extinction from our UV selection, provided that we account for dust extinction. This holds true despite the inherent uncertainties associated with attenuating UV galaxies.

6 CONCLUSION

In this work, we investigate the dust properties of a sample of UV-selected galaxies from the Chandra deep field south (CDFS) in the redshift range 0.6 – 1.2. The sample under consideration comprises 1070 galaxies, with a magnitude range of $M_{UV} = [-21.15, -19.0]$, after removing the UV LF bins containing < 25 sources. This conservative cut makes sure we have robust enough statistics for our calculations. To assess the average FIR properties of this UV-selected sample, we make use of the FIR maps of the CDFS, generated by the *Herschel* Multi-tiered Extragalactic Survey (HerMES). The FIR maps are created on the basis of observations from the PACS and SPIRE instruments onboard *Herschel*.

We stack the UV sources from the CDFS dataset onto the FIR maps obtained from *Herschel*-PACS at 100 and 160 μm , as well as *Herschel*-SPIRE at 250, 350 and 500 μm , in order to determine the average flux densities as a function of the redshift and UV luminosity binned according to the UV LF of these galaxies. Prior to stacking, we deblend the FIR maps to mitigate the effects of blending and confusion of sources in the *Herschel* IR maps. Using the stacked fluxes, we determined the average dust temperature and total FIR luminosities (from 8-1000 μm) for the galaxies in each bin of the UV LF. These FIR luminosities, along with the UV luminosities, are then employed to estimate the dust attenuation of the galaxies and to characterise the evolution of the comoving SFR density between redshifts 0.6 – 1.2. The primary conclusions derived from our study can be summarised as follows:

1. The IR luminosities of our UV-selected sources are on average in the range 2.15×10^{10} to $6.5 \times 10^{10} L_{\odot}$, placing them in the sub-LIRG category. We find that the typical luminosity-weighted dust temperatures at redshifts 0.7 and 1.0 are 30.28 ± 1.33 K and 33.12 ± 1.26 K, respectively. We have not observed any significant trends between the average dust temperatures and integrated IR luminosities of these galaxies at a fixed redshift. Furthermore, our analysis of the temperature (averaged over the UV LF bins) within the redshift range explored in our study has revealed no significant variation in the redshift range of our study. However, it is important to remark here that this study explores a rather limited range in redshift space. When we add data from other studies conducted in the redshift range of 0.1 to 1.5, our values agree with a weak trend between these parameters observed in previous studies.

2. Our UV-selected galaxies have median dust obscuration levels of $\text{IRX} = 3.17 \pm 0.52$ and 3.49 ± 0.51 , which correspond to dust attenuation of 1.15 ± 0.24 and 1.22 ± 0.23 magnitudes, at redshifts 0.7 and 1.0, respectively. We did not find any changes in the dust attenuation within the redshift range covered by our study, which suggests that the dust content in UV-selected star-forming galaxies does not evolve very much between redshifts of 1.0 to 0.7. We do observe a pattern in the values of IRX with IR luminosity, wherein the IRX decreases as the IR luminosity increases for a constant redshift. However, the trend is very weak and cannot be substantiated due to the small range of IR luminosities covered in this study. No significant trends are detected between IRX and redshift at a constant IR luminosity. However, in the case of local galaxies, there is a positive correlation between IRX and IR luminosity. We speculate that this difference may be due to selection bias. We see an increase in IRX with decreasing UV luminosity.

3. It is observed that the SFR calculated using UV indicators is underestimated by a factor of 3 at redshifts of 0.7 and 1.0 compared to the total SFR. This offset decreases as the UV luminosity increases for both redshift bins. This indicates that the dust obscuration decreases as the UV luminosity of the galaxies increases, within the range analysed in this study. It has also been found that the relationship between IRX and bolometric luminosity remains unchanged from redshift 1 to 0.7. The IRX exhibits a roughly constant trend with increasing bolometric luminosity, which is in agreement with the local relations for UV-selected galaxies, where these quantities show a weak correlation within

the luminosity range of our sources. Overall, the results are consistent with the proposed picture from previous studies that the UV-selected galaxies at higher redshifts exhibit a lesser degree of dust attenuation at a fixed bolometric luminosity compared to those in the local Universe. However, we did not observe any evolution of the dust attenuation at a given bolometric luminosity from redshift 0.7 to 1 in our sample.

4. We did not find any significant change in the SFR density with the redshift changing from 1.0 to 0.7. The values at both our redshifts agree reasonably well with previous investigations. The ratio of the obscured to the total star formation is in the 65-70 per cent range.

7 ACKNOWLEDGEMENTS

This research makes use of observations taken with the *Herschel* observatory. *Herschel* is an ESA space observatory with science instruments provided by European-led Principal Investigator consortia and with important participation from NASA. This research has used data from the HerMES project (<http://hermes.sussex.ac.uk>). HerMES is a *Herschel* Key Programme utilising Guaranteed Time from the SPIRE instrument team, ESAC scientists, and a mission scientist. The HerMES data were accessed through the *Herschel* Database in Marseille (HeDaM - <http://hedam.lam.fr>) operated by CeSAM and hosted by the Laboratoire d'Astrophysique de Marseille. MS thanks Unnikrishnan Sureshkumar for the help and discussions regarding the calculation of the angular correlation functions used in this work. MS also extends their gratitude to Benjamin Magnelli for providing the MIPS-24 μm /70 μm ECDFS FIDEL data. We thank the referee Tom Bakx for their constructive report which further improved this manuscript.

8 DATA AVAILABILITY

The *Herschel* maps used in this paper can be obtained from the HeDaM database available at <https://hedam.lam.fr/HerMES/index/dr4> and the PEP pages at <https://www.mpe.mpg.de/ir/Research/PEP/DR1>. The UVW1 source list is provided as the supplementary Table with the online version of our previous study Sharma et al. (2022). Other supporting material related to this article is available on a reasonable request to the corresponding author.

REFERENCES

- Álvarez-Márquez J., et al., 2016, *A&A*, **587**, A122
 Arnouts S., et al., 2005, *ApJ*, **619**, L43
 Bell E. F., 2003, *ApJ*, **586**, 794
 Bertin E., Arnouts S., 1996, *A&AS*, **117**, 393
 Béthermin M., Dole H., Cousin M., Bavouzet N., 2010, *A&A*, **516**, A43
 Béthermin M., et al., 2012, *A&A*, **542**, A58
 Béthermin M., et al., 2015, *A&A*, **573**, A113
 Blain A. W., Barnard V. E., Chapman S. C., 2003, *MNRAS*, **338**, 733
 Boquien M., Salim S., 2021, *A&A*, **653**, A149
 Bouwens R. J., et al., 2009, *ApJ*, **705**, 936
 Bouwens R. J., et al., 2012, *ApJ*, **754**, 83

- Bouwens R. J., et al., 2015, *ApJ*, **803**, 34
- Bouwens R., et al., 2020, *ApJ*, **902**, 112
- Buat V., 1992, *A&A*, **264**, 444
- Buat V., Xu C., 1996, *A&A*, **306**, 61
- Buat V., Donas J., Milliard B., Xu C., 1999, *A&A*, **352**, 371
- Buat V., et al., 2005, *ApJ*, **619**, L51
- Buat V., et al., 2007a, *ApJS*, **173**, 404
- Buat V., Marcillac D., Burgarella D., Le Floch E., Takeuchi T. T., Iglesias-Parámo J., Xu C. K., 2007b, *A&A*, **469**, 19
- Buat V., Takeuchi T. T., Burgarella D., Giovannoli E., Murata K. L., 2009, *A&A*, **507**, 693
- Budavári T., et al., 2005, *ApJ*, **619**, L31
- Burgarella D., Buat V., Iglesias-Parámo J., 2006, *MNRAS*, **365**, 352
- Burgarella D., Le Floch E., Takeuchi T. T., Huang J. S., Buat V., Rieke G. H., Tyler K. D., 2007, *MNRAS*, **380**, 986
- Burgarella D., et al., 2013, *A&A*, **554**, A70
- Calzetti D., Kinney A. L., Storchi-Bergmann T., 1994, *ApJ*, **429**, 582
- Calzetti D., Armus L., Bohlin R. C., Kinney A. L., Koornneef J., Storchi-Bergmann T., 2000, *ApJ*, **533**, 682
- Calzetti D., et al., 2007, *ApJ*, **666**, 870
- Casey C. M., et al., 2011, *MNRAS*, **415**, 2723
- Casey C. M., et al., 2014, *ApJ*, **796**, 95
- Casey C. M., et al., 2018, *ApJ*, **862**, 77
- Chapin E. L., et al., 2011, *MNRAS*, **411**, 505
- Chapman S. C., Smail I., Ivison R. J., Helou G., Dale D. A., Lagache G., 2002, *ApJ*, **573**, 66
- Chapman S. C., Helou G., Lewis G. F., Dale D. A., 2003, *ApJ*, **588**, 186
- Cortese L., Boselli A., Franzetti P., Decarli R., Gavazzi G., Boissier S., Buat V., 2008, *MNRAS*, **386**, 1157
- Cucciati et al., 2012, *A&A*, **539**, A31
- Dale D. A., Helou G., Contursi A., Silbermann N. A., Kolhatkar S., 2001, *ApJ*, **549**, 215
- Dole H., et al., 2006, *A&A*, **451**, 417
- Donnan C. T., et al., 2023, *MNRAS*, **518**, 6011
- Draine B. T., Li A., 2007, *ApJ*, **657**, 810
- Drew P. M., Casey C. M., 2022, *ApJ*, **930**, 142
- Dunne L., Eales S., Edmunds M., Ivison R., Alexander P., Clements D. L., 2000, *MNRAS*, **315**, 115
- Finkelstein S. L., et al., 2012, *ApJ*, **756**, 164
- Franzen T. M. O., et al., 2015, *MNRAS*, **453**, 4020
- Fudamoto Y., et al., 2020, *MNRAS*, **491**, 4724
- Genzel R., et al., 1998, *ApJ*, **498**, 579
- Gordon K. D., Clayton G. C., Witt A. N., Misselt K. A., 2000, *ApJ*, **533**, 236
- Griffin M. J., et al., 2010, *A&A*, **518**, L3
- Gruppioni C., et al., 2013, *MNRAS*, **432**, 23
- Hagen L. M. Z., Hoversten E. A., Gronwall C., Wolf C., Siegel M. H., Page M., Hagen A., 2015, *ApJ*, **808**, 178
- Hao C.-N., Kennicutt R. C., Johnson B. D., Calzetti D., Dale D. A., Moustakas J., 2011, *ApJ*, **741**, 124
- Heckman T. M., Robert C., Leitherer C., Garnett D. R., van der Rydt F., 1998, *ApJ*, **503**, 646
- Heinis S., et al., 2013, *MNRAS*, **429**, 1113
- Hopkins A. M., Beacom J. F., 2006, *ApJ*, **651**, 142
- Hwang H. S., et al., 2010, *MNRAS*, **409**, 75
- Iglesias-Parámo J., et al., 2006, *ApJS*, **164**, 38
- Kennicutt Robert C. J., 1998, *ARA&A*, **36**, 189
- Kennicutt R. C., Evans N. J., 2012, *ARA&A*, **50**, 531
- Kirkpatrick A., et al., 2012, *ApJ*, **759**, 139
- Kirkpatrick A., et al., 2017, *ApJ*, **843**, 71
- Kroupa P., 2001, *MNRAS*, **322**, 231
- Kurczynski P., Gawiser E., 2010, *AJ*, **139**, 1592
- Kurczynski P., et al., 2014, *ApJ*, **793**, L5
- Le Floch E., et al., 2005, *ApJ*, **632**, 169
- Lee K.-S., Alberts S., Atlee D., Dey A., Pope A., Jannuzi B. T., Reddy N., Brown M. J. L., 2012, *ApJ*, **758**, L31
- Liang L., et al., 2019, *MNRAS*, **489**, 1397
- Liu D., et al., 2018, *ApJ*, **853**, 172
- Luo B., et al., 2008, *ApJS*, **179**, 19
- Lutz D., et al., 2011, *A&A*, **532**, A90
- Madau P., Dickinson M., 2014, *ARA&A*, **52**, 415
- Magdis G. E., et al., 2012, *ApJ*, **760**, 6
- Magnelli B., Elbaz D., Chary R. R., Dickinson M., Le Borgne D., Frayer D. T., Willmer C. N. A., 2011, *A&A*, **528**, A35
- Magnelli B., et al., 2013, *A&A*, **553**, A132
- Magnelli B., et al., 2014, *A&A*, **561**, A86
- Marsden G., et al., 2009, *ApJ*, **707**, 1729
- Mason K. O., et al., 2001, *A&A*, **365**, L36
- Meurer G. R., Heckman T. M., Leitherer C., Kinney A., Robert C., Garnett D. R., 1995, *AJ*, **110**, 2665
- Meurer G. R., Heckman T. M., Calzetti D., 1999, *ApJ*, **521**, 64
- Miller N. A., et al., 2013, *ApJS*, **205**, 13
- Moutard T., Sawicki M., Arnouts S., Golob A., Coupon J., Ilbert O., Yang X., Gwyn S., 2020, *MNRAS*, **494**, 1894
- Murphy E. J., et al., 2011, *ApJ*, **737**, 67
- Narayanan D., Davé R., Johnson B. D., Thompson R., Conroy C., Geach J., 2018, *MNRAS*, **474**, 1718
- Nguyen H. T., et al., 2010, *A&A*, **518**, L5
- Nordon R., et al., 2013, *ApJ*, **762**, 125
- Oesch P. A., et al., 2010, *ApJ*, **725**, L150
- Oesch P. A., et al., 2018, *ApJS*, **237**, 12
- Oke J. B., Gunn J. E., 1983, *ApJ*, **266**, 713
- Oliver S. J., et al., 2012, *MNRAS*, **424**, 1614
- Overzier R. A., et al., 2010, *The Astrophysical Journal*, **726**, L7
- Page M. J., et al., 2021, *MNRAS*, **506**, 473
- Parsa S., Dunlop J. S., McLure R. J., Mortlock A., 2016, *MNRAS*, **456**, 3194
- Pilbratt G. L., et al., 2010, *A&A*, **518**, L1
- Poglitsch A., et al., 2010, *A&A*, **518**, L2
- Reddy N. A., Steidel C. C., Erb D. K., Shapley A. E., Pettini M., 2006, *ApJ*, **653**, 1004
- Reddy N. A., Erb D. K., Pettini M., Steidel C. C., Shapley A. E., 2010, *ApJ*, **712**, 1070
- Reddy N., et al., 2012, *ApJ*, **744**, 154
- Reddy N. A., et al., 2018, *ApJ*, **853**, 56
- Rosati P., et al., 2002, *ApJ*, **566**, 667
- Roseboom I. G., et al., 2012, *MNRAS*, **419**, 2758
- Salpeter E. E., 1955, *ApJ*, **121**, 161
- Sanders D. B., Mirabel I. F., 1996, *ARA&A*, **34**, 749
- Schiminovich D., et al., 2005, *ApJ*, **619**, L47
- Schreiber C., Elbaz D., Pannella M., Ciesla L., Wang T., Franco M., 2018, *A&A*, **609**, A30
- Seibert M., et al., 2005, *ApJ*, **619**, L55
- Sharma M., Page M. J., Breeveld A. A., 2022, *MNRAS*, **511**, 4882
- Sharma M., Page M. J., Ferreras I., Breeveld A. A., 2023, ([arXiv:2212.00215](https://arxiv.org/abs/2212.00215))
- Skelton R. E., et al., 2014, *ApJS*, **214**, 24
- Soifer B. T., Neugebauer G., Houck J. R., 1987, *ARA&A*, **25**, 187
- Steidel C. C., Shapley A. E., Pettini M., Adelberger K. L., Erb D. K., Reddy N. A., Hunt M. P., 2004, *The Astrophysical Journal*, **604**, 534
- Sullivan M., Treyer M. A., Ellis R. S., Bridges T. J., Milliard B., Donas J., 2000, *MNRAS*, **312**, 442
- Swinbank A. M., et al., 2014, *MNRAS*, **438**, 1267
- Symeonidis M., Page M. J., 2019, *MNRAS*, **485**, L11
- Symeonidis M., Page M. J., 2021, *MNRAS*, **503**, 3992
- Symeonidis M., Page M. J., Seymour N., Dwelly T., Coppin K., McHardy I., Rieke G. H., Huynh M., 2009, *MNRAS*, **397**, 1728
- Symeonidis M., et al., 2013, *MNRAS*, **431**, 2317
- Takeuchi T. T., Buat V., Burgarella D., 2005, *A&A*, **440**, L17
- Thomson A. P., et al., 2017, *ApJ*, **838**, 119
- Tress M., et al., 2018, *MNRAS*, **475**, 2363

- Viero M. P., et al., 2012, *MNRAS*, **421**, 2161
Viero M. P., et al., 2013, *ApJ*, **779**, 32
Wilkins S. M., Bunker A. J., Stanway E., Lorenzoni S., Caruana J., 2011, *MNRAS*, **417**, 717
Wilkins S. M., Gonzalez-Perez V., Lacey C. G., Baugh C. M., 2012a, *MNRAS*, **424**, 1522
Wilkins S. M., Gonzalez-Perez V., Lacey C. G., Baugh C. M., 2012b, *MNRAS*, **427**, 1490
Wilkins S. M., Bunker A., Coulton W., Croft R., di Matteo T., Khandai N., Feng Y., 2013, *MNRAS*, **430**, 2885
Witt A. N., Gordon K. D., 2000, *ApJ*, **528**, 799
Wyder T. K., et al., 2005, *ApJ*, **619**, L15
Xu C., Buat V., 1995, *A&A*, **293**, L65
Xu C. K., et al., 2007, *ApJS*, **173**, 432
Zheng X. Z., Dole H., Bell E. F., Le Flo'c'h E., Rieke G. H., Rix H.-W., Schiminovich D., 2007, *ApJ*, **670**, 301

APPENDIX A: DEBLENDED MAPS AND STACKS

Here we show the deblending process for 350 and 500 μm maps from *Herschel* SPIRE in Figure A1. These maps are produced as explained in Section 3.

This paper has been typeset from a $\text{T}_{\text{E}}\text{X}/\text{L}^{\text{A}}\text{T}_{\text{E}}\text{X}$ file prepared by the author.

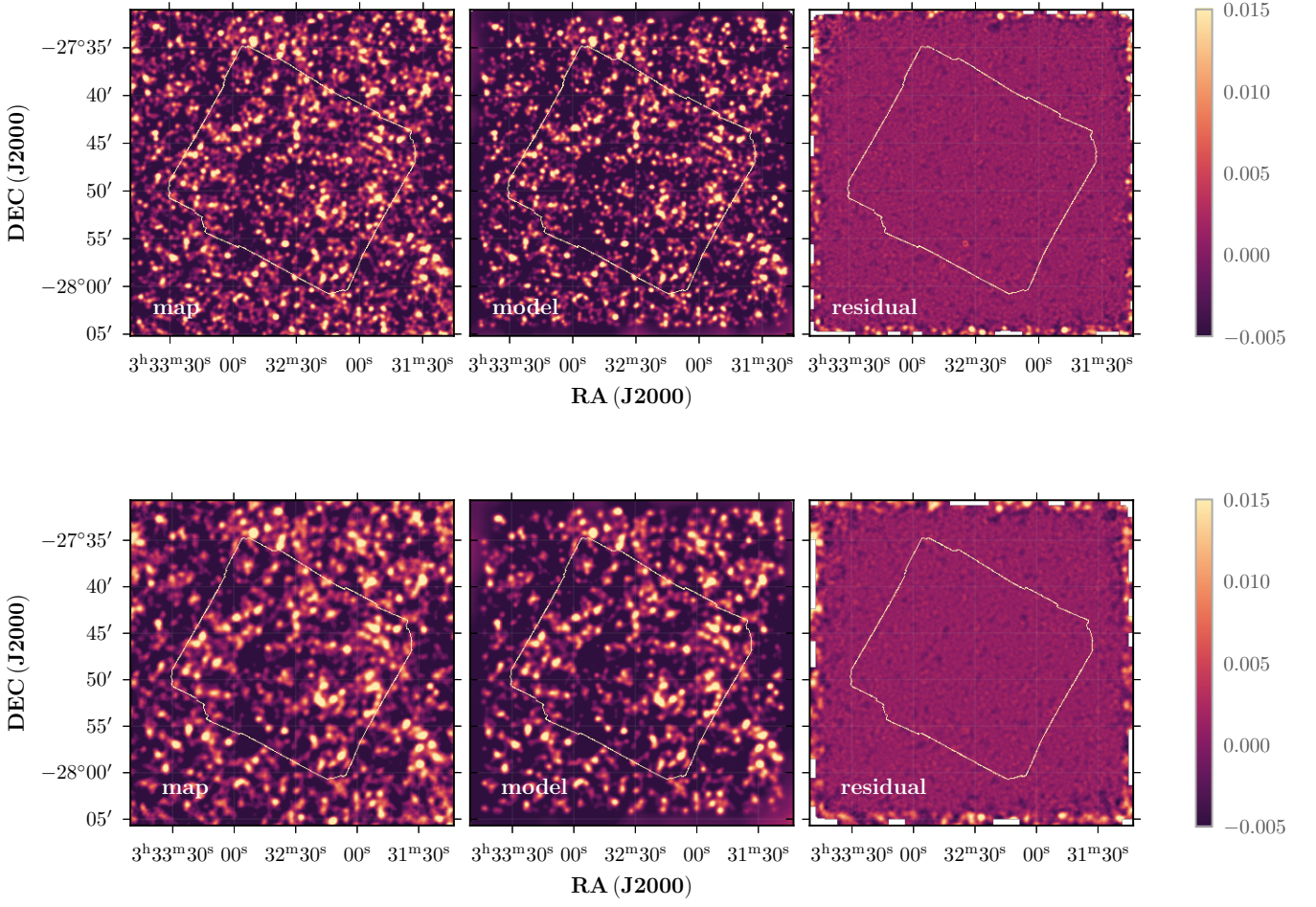


Figure A1. The deblending process as described in Section 3 for the 350 and 500 μm maps from *Herschel* SPIRE. The arrangement of the panels is the same as in Figure 3.